Autism-like behavior caused by deletion of vaccinia-related kinase 3 is improved by TrkB stimulation

Myung-Su Kang,[1] Tae-Yong Choi,[3] Hye Guk Ryu,[1] Dohyun Lee,[1] Seung-Hyun Lee,[3] Se-Young Choi,[3] and Kyong-Tai Kim[1,2]

[1]Department of Life Sciences and [2]Division of Integrative Biosciences and Biotechnology, Pohang University of Science and Technology, Pohang, Republic of Korea
[3]Department of Physiology, Dental Research Institute, Seoul National University School of Dentistry, Seoul, Republic of Korea

Vaccinia-related kinases (VRKs) are multifaceted serine/threonine kinases that play essential roles in various aspects of cell signaling, cell cycle progression, apoptosis, and neuronal development and differentiation. However, the neuronal function of *VRK3* is still unknown despite its etiological potential in human autism spectrum disorder (ASD). Here, we report that *VRK3*-deficient mice exhibit typical symptoms of autism-like behavior, including hyperactivity, stereotyped behaviors, reduced social interaction, and impaired context-dependent spatial memory. A significant decrease in dendritic spine number and arborization were identified in the hippocampus CA1 of *VRK3*-deficient mice. These mice also exhibited a reduced rectification of AMPA receptor–mediated current and changes in expression of synaptic and signaling proteins, including tyrosine receptor kinase B (TrkB), Arc, and CaMKIIα. Notably, TrkB stimulation with 7,8-dihydroxyflavone reversed the altered synaptic structure and function and successfully restored autism-like behavior in *VRK3*-deficient mice. These results reveal that *VRK3* plays a critical role in neurodevelopmental disorders and suggest a potential therapeutic strategy for ASD.

INTRODUCTION

Vaccinia-related kinases (VRKs) belong to the casein kinase family, whose catalytic domain shares sequence homology with the vaccinia virus gene B1R. VRKs are multifaceted serine/threonine kinases that play essential roles in many aspects of cell signaling, cell cycle progression, nuclear envelope dynamics, histone modification, and apoptosis (Kang and Kim, 2006; Klerkx et al., 2009; Park et al., 2015). Abnormal VRK functions result in various diseases. Dysregulation of *VRK1* and *VRK2* is reported to cause spinal muscular atrophies and schizophrenia, respectively (Renbaum et al., 2009; Sohn et al., 2014).

VRK3, one of the VRK subtypes, is highly expressed during development and promotes cell cycle progression by phosphorylating the nuclear envelope protein BAF (barrier to autointegration factor; Park et al., 2015). *VRK3* decreases extracellular signal-regulated kinase (ERK) activity through direct binding to a mitogen-activated protein kinase phosphatase, vaccinia H1-related, which specifically inactivates *ERK* in the nucleus (Kang and Kim, 2006). ERKs are hub kinases that activate various signaling pathways in many types of cells, including neurons (Flavell and Greenberg, 2008). Neuronal ERK signaling is involved in the regulation of synaptic protein synthesis, dendritic morphology, and functional plasticity (Wu et al., 2001; Thomas and Huganir, 2004; Kelleher and Bear, 2008). Dysregulation of ERK signaling can result in autism spectrum disorder (ASD; Faridar et al., 2014; Subramanian et al., 2015; Yufune et al., 2015). Notably, deletion or duplication of chromosomal locus 16p11.2, which includes the *ERK1* gene, is commonly associated with ASD (Qureshi et al., 2014).

As a modulator of ERK signaling, *VRK3* is also thought to play a critical role in neuronal function. Amyloid-β oligomers induce a down-regulation of *VRK3*, which could contribute to synaptic dysfunction in Alzheimer's disease (Sebollela et al., 2012). Interestingly, copy-number variants (CNVs) at the 19q13.33 region, which includes the *VRK3* gene (NM_016440), are associated with ASD and other intellectual disabilities (Firth et al., 2009; Xu et al., 2012). However, the synaptic function of *VRK3* is still unknown, although the role of *VRK3* in synaptic structure and function is critical to understand the etiology of ASD caused by *VRK3* mutations.

In this study, by generating *VRK3*-deleted mice with a reporter in the *VRK3* intron region, we explored whether *VRK3* deletion causes symptoms similar to those of psychiatric disorders in humans and investigated the mechanisms underlying this effect. We found that *VRK3*-knockout (*VRK3*-KO) mice exhibited autism-like behaviors as well as altered synaptic structure and function. Also, we found that

Correspondence to Kyong-Tai Kim: ktk@postech.ac.kr; Se-Young Choi: sychoi@snu.ac.kr

Abbreviations used: 7,8-DHF, 7,8-dihydroxyflavone; ACSF, artificial cerebrospinal fluid; ASD, autism spectrum disorder; CNV, copy-number variant; DG, dentate gyrus; EPM, elevated plus maze; EPSC, excitatory postsynaptic current; ERK, extracellular signal-regulated kinase; LTD, long-term depression; LTP, long-term potentiation; mEPSC, miniature EPSC; mIPSC, miniature inhibitory postsynaptic current; PSD, postsynaptic density; SC, Schaffer collateral; sEPSC, spontaneous EPSC; sIPSC, spontaneous inhibitory postsynaptic current; SynGAP, synaptic GTPase-activating protein; VRK, vaccinia-related kinase.

The Rockefeller University Press
J. Exp. Med. 2017 Vol. 214 No. 10 2947–2966
https://doi.org/10.1084/jem.20160974

activation of the tyrosine receptor kinase B (TrkB) signaling pathway alleviated these abnormalities in *VRK3*-KO animals.

RESULTS

VRK3-KO mice exhibit autism-like behavior

In the present study, we generated *VRK3*-depleted mice (Fig. S1 A). The deletion mutation between exons 7 and 8 was verified using various PCR methods (Fig. 1, A and B). Loss of full-length VRK3 protein was verified by Western blot (Fig. 1 C). The gene trap insertion sites on VRK3 protein are shown in Fig. S1 B. We first sought to determine whether *VRK3*-KO mice displayed unusual social interactions and repetitive behaviors, which are core symptoms of ASD. Both *VRK3*-KO and WT mice had no preference for the right and the left chambers during a habituation period (Fig. 1 D). However, *VRK3*-KO mice did not show any preference for exploring a novel mouse-containing cage over a novel empty cage in a three-chamber test (Fig. 1 E). When a novel mouse was placed in the empty cage to assess discrimination between new and familiar mice, *VRK3*-KO mice showed no significant preference for exploring the novel mouse (Fig. 1 F). *VRK3*-KO mice exhibited longer durations of grooming behavior (Fig. 1 G). To explore maternal care on pup behavior, we measured latency for pup retrieval from a scattered nest and found that *VRK3*-KO female mice retrieved pups less efficiently than WT mice (Fig. 1 H). In addition, *VRK3*-KO mice also performed less efficiently than WT mice in a nesting behavior assay (Fig. 1 I). These results suggest that *VRK3*-KO mice display unusual social interactions and autism-related behavioral abnormalities.

Decreased *VRK3* weakened hippocampus-dependent cognitive functions, including spatial learning and memory

We next analyzed other cognitive defects in *VRK3*-KO animals. *VRK3*-KO mice showed shorter step-through latencies than WT mice after experiencing electric shock in a dark room (Fig. 2 A). In a novel object recognition test, *VRK3*-KO mice exhibited a reduced ability to discriminate between familiar and novel objects at 24 h after training (Fig. 2 B). The Barnes circular maze test also showed that *VRK3*-KO mice had significantly impaired spatial memory compared with WT mice without a change in exploratory behavior after 4 d of training (Fig. 2 C). In an open-field test, *VRK3*-KO mice displayed hyperactivity and anxiolytic behavior (Fig. 2 D), which were confirmed by the results obtained from elevated plus maze (EPM) and light–dark exploration test, yet the distance moved in the EPM remained normal (Fig. 2, E and F). These data suggest that *VRK3*-KO mice have impaired cognitive functions, including spatial learning and memory as well as anxiolytic behavior. In addition, *VRK3*-heterozygous mice exhibited anxiolytic behavior and hyperactivity (Fig. S2, A and B) along with reduced performance in novel object recognition test (Fig. S2 C). *VRK3*-heterozygous mice also revealed impaired learning and memory performance in Barnes circular maze test (Fig. S2 D).

VRK3-KO mice show decreased spine number and arborization as well as abnormal PSD

Next, we examined the morphology of dendritic spines in the hippocampus (Fig. 3, A and F). *VRK3*-KO mice exhibited significant reductions in spine density in the CA1 (Fig. 3 B) and dentate gyrus (DG) regions (Fig. 3 G). In the CA1 region, reductions in spine density were more prominent on basal dendrites than apical dendrites in *VRK3*-KO animals (Fig. 3 B). Interestingly, the length of dendritic spines was markedly increased in all spine types of the CA1 region (Fig. 3 C), whereas it was not changed in the DG region of *VRK3*-KO animals (Fig. 3 I). We found similar proportions of all types of dendritic spines in the CA1 and DG regions between WT and *VRK3*-KO mice (Fig. 3, E and J). We further analyzed postsynaptic density (PSD) in hippocampal CA1 regions using electron microscopy (Fig. 3 K), which revealed prominent reductions in PSD length and thickness in *VRK3*-KO mice (Fig. 3, L and M). We also found decreased dendritic arborization in *VRK3*-KO animals with Sholl analysis (Fig. 3, N and O). These results suggest alterations in dendritic spines and concomitant decreases of PSD structure in hippocampus of *VRK3*-KO animals.

VRK3-KO mice show a decreased proportion of Ca^{2+}-permeable AMPA receptors

We characterized the synaptic transmission and plasticity in *VRK3*-KO mice. The amplitude and frequency of miniature excitatory postsynaptic currents (mEPSCs; Fig. 4 A), miniature inhibitory postsynaptic currents (mIPSCs; Fig. 4 B), spontaneous excitatory postsynaptic currents (sEPSCs; Fig. S3 A) and spontaneous inhibitory postsynaptic currents (sIPSCs; Fig. S3 B) were identical in WT and *VRK3*-KO mice in pyramidal cells of the hippocampal CA1 region. The input–output relationship for the CA3–CA1 Schaffer collateral (SC) circuit of *VRK3*-KO mice was also normal (Fig. S3 C). Theta-burst stimulation induced NMDA receptor–dependent long-term potentiation (LTP; Fig. 4 C) was also normal in in *VRK3*-KO mice. We tested two types of long-term depression (LTD) induction: single-pulse stimulation induced NMDA receptor–dependent LTD and DHPG-induced metabotropic glutamate receptor–dependent LTD. However, both forms of LTD are intact in *VRK3*-KO mice (Fig. 4 D and Fig. S3 D). Moreover, *VRK3*-KO mice showed normal intrinsic excitability of hippocampal CA1 pyramidal cells (Fig. 4 E), paired-pulse ratio (Fig. 4 F), and 20-Hz-train stimulation-mediated excitatory postsynaptic current (EPSC) response (Fig. 4 H), implying intact presynaptic neurotransmitter release in *VRK3*-KO animals. The ratio between AMPA and NMDA receptor activity was the same in WT and *VRK3*-KO mice (Fig. 4 G). Notably, however, the ratio of AMPA receptor–mediated currents measured at 40 and −70 mV holding potentials (also known as rectification) was decreased in *VRK3*-KO mice (Fig. 4, I and J), suggesting a decreased proportion of Ca^{2+}-permeable AMPA receptor in *VRK3*-KO mice.

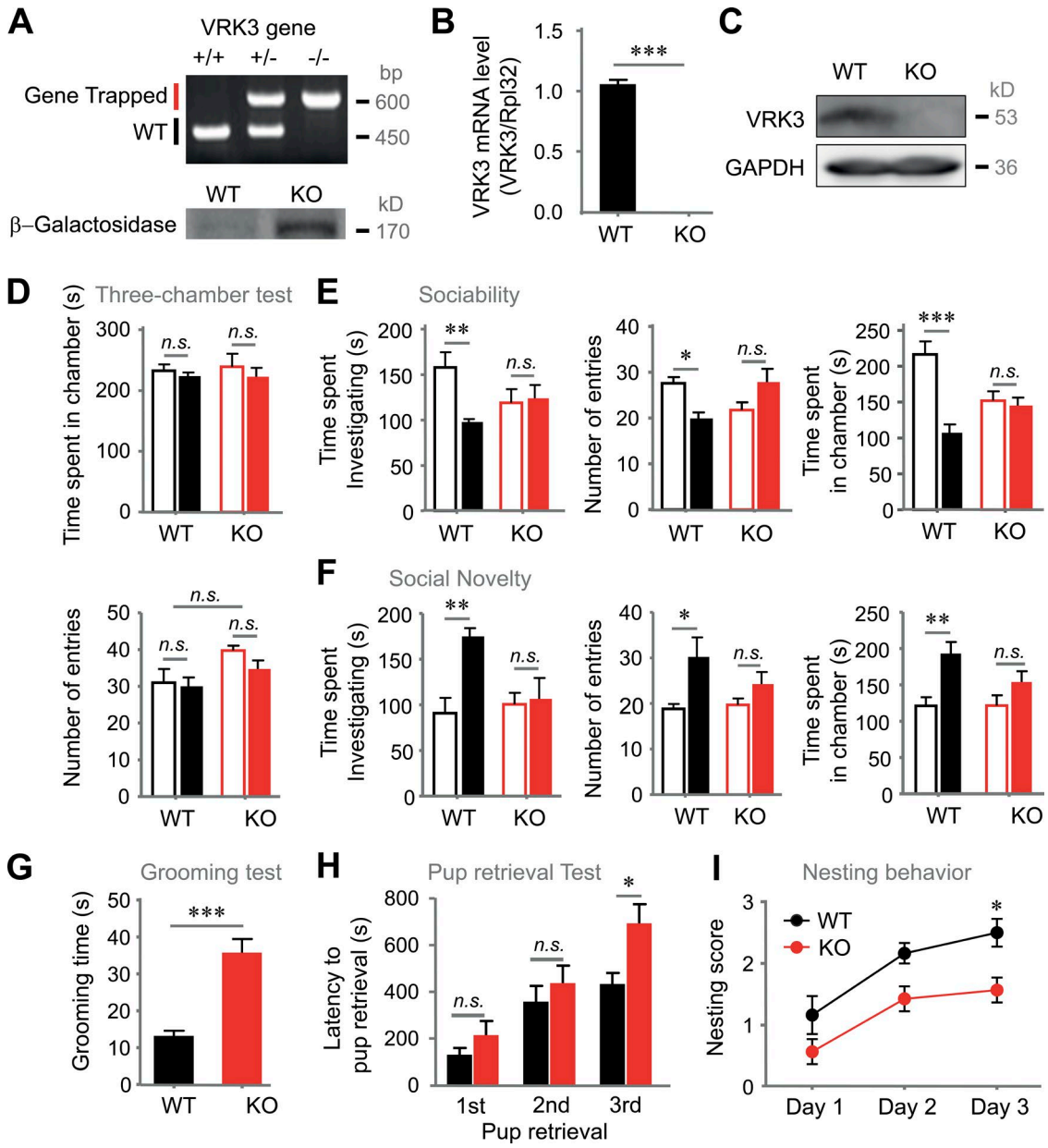

Figure 1. ***VRK3*-KO mice exhibit autism-like behavior.** (A) Genotypes of *VRK3*-knockout (*VRK3*-KO) mice were determined by PCR of tail DNA, and verification of *VRK3*-KO mice, which contain a gene encoding β-galactosidase, was performed by Western blot analysis. (B) *VRK3* mRNA level was quantified by real-time RT-PCR. *VRK3* mRNA level was normalized to Rpl32 mRNA level (n = 7, 7 for WT and *VRK3*-KO mice, respectively; t_{12} = 27.45, ***, P < 0.001, *t* test). (C) Western blot probed with an antibody directed against *VRK3*. Full-length VRK3 protein is absent in *VRK3*-KO mice. (D) The preference for either side of the three-chamber unit in the habituation period (n = 5, 5), and time spent (top) and number of entries (bottom) for the left (blank bar) and right chamber (filled bar) of the three-chamber unit. (E) Sociability (mouse 1 [blank bar] versus object [filled bar]) in a three-chamber assay, time spent investigating (left; n = 5, 5; interaction $F_{1,8}$ = 5.37, two-way ANOVA; **, P < 0.01, P > 0.05, Bonferroni's post-test), total number of entries (middle; n = 11, 13; interaction $F_{1,44}$ = 10.81, P = 0.002, two-way ANOVA; *, P < 0.05, P > 0.05, Bonferroni's post-test), and time spent in each chamber (right; n = 11, 13; WT vs. *VRK3* KO $F_{1,44}$ = 18.36, P < 0.0001, interaction $F_{1,44}$ = 14.25, P = 0.0005, two-way ANOVA; ***, P < 0.001, P > 0.05, Bonferroni's post-test). (F) Preference for social novelty (familiar mouse [blank bar] vs. novel mouse [filled bar] in a three-chamber assay, time spent investigating (left; n = 5, 5; WT vs. *VRK3* KO $F_{1,8}$ = 7.68, *, P < 0.05, interaction $F_{1,8}$ = 5.82, *, P < 0.05, two-way ANOVA; **, P < 0.01, P > 0.05, Bonferroni's post-test), total number of entries (middle; n = 11, 13; WT vs. *VRK3* KO $F_{1,44}$ = 9.50; **, P < 0.01; two-way ANOVA; *, P < 0.05, P > 0.05, Bonferroni's post-test), and time spent in each chamber (right; n = 11, 13; WT vs. *VRK3* KO $F_{1,44}$ = 13.00, P = 0.0008, two-way ANOVA; **, P < 0.01, P > 0.05, Bonferroni's post-test). (G) Duration of repetitive behavior in a grooming task (n = 11, 13; t_{22} = 5.369, ***, P < 0.001, *t* test). (H) Latency to pup retrieval (n = 6, 7; WT vs. *VRK3*-KO female mice $F_{2,33}$ = 18.35, P < 0.0001, two-way ANOVA; *, P < 0.05, Bonferroni's post-test). (I) Nest-building index over 3 d of a nesting behavior test (n = 6, 7; WT vs. *VRK3* KO $F_{2,33}$ = 15.72, P < 0.0001, two-way ANOVA; *, P < 0.05, Bonferroni's post-test). n.s., not significant. All values represent mean ± SEM.

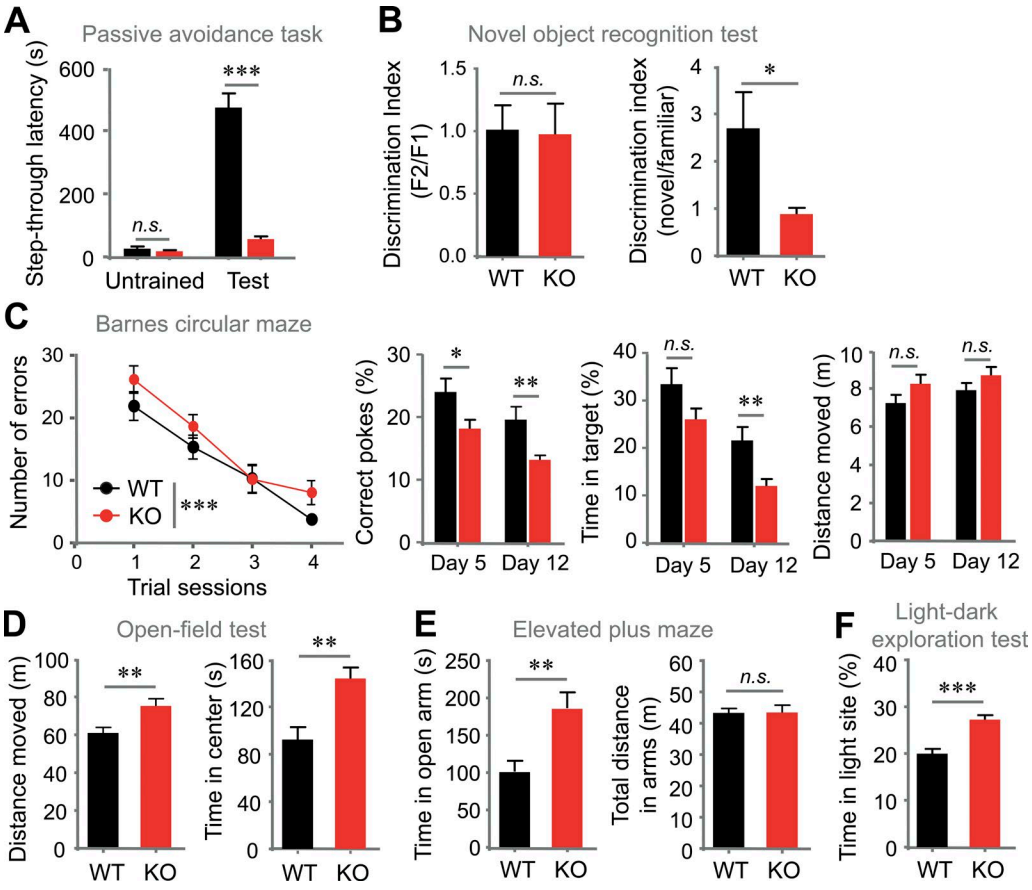

Figure 2. ***VRK3*-KO mice exhibit impaired learning and memory and abnormal behavior.** (A) Passive avoidance. Step-through latencies into the dark compartment before (untrained) and 2 d after foot shock (test; $n = 14, 15$ for WT and *VRK3*-KO mice, respectively; WT vs. *VRK3* KO $F_{1,54} = 115.63$, $P < 0.0001$, untrained vs. test $F_{1,54} = 88.63$, $P < 0.0001$; interaction $F_{1,54} = 82.15$, $P < 0.0001$, two-way ANOVA; $P > 0.05$, ***, $P < 0.001$, Bonferroni's post-test). (B) The novel object recognition test with discrimination index for a familiar objects (left; F1, familiar 1; F2, familiar 2), which was presented 24 h before the test ($n = 5, 5$; $P > 0.05$, *t* test), and discrimination index for novel object recognition ability (right; $n = 5, 5$; *, $P < 0.05$, *t* test). (C) Barnes circular maze with number of errors across each day of training (left; $n = 15, 15$; trial sessions $F_{1,110} = 4.35$, $P < 0.05$; genotype $F_{3,110} = 32.30$, $P < 0.0001$, two-way ANOVA; $P > 0.05$, Bonferroni's post-test). Probe test on the fifth and 12th day of training with correct pokes (middle left; $n = 14, 14$ for WT and *VRK3*-KO mice; day 5 vs. day 12, $F_{1,45} = 7.90$, $P < 0.01$; WT vs. *VRK3* KO, $F_{1,45} = 13.44$, $P < 0.001$, two-way ANOVA; *, $P < 0.05$; **, $P < 0.01$; ***, $P < 0.001$, Bonferroni's post-test), and time in target (middle right; $n = 14, 14$; day 5 vs. day 12, $F_{1,45} = 11.45$, $P < 0.01$; WT vs *VRK3* KO, $F_{1,45} = 26.46$, $P < 0.0001$, two-way ANOVA; **, $P < 0.01$, Bonferroni's post-test), and distance moved (right; $n = 14, 14$; $P > 0.05$, *t* test). (D) Total locomotor activity (left) and time spent in the center region (right) of the open field ($n = 11, 14$; **, $P < 0.01$, *t* test). (E) Time spent in open arms (left) and total locomotor activity (right) in the elevated plus maze ($n = 12, 12$; **, $P < 0.01$, $P > 0.05$, *t* test). (F) Duration of time spent in the light compartment in the light-dark exploration test ($n = 12, 14$; ***, $P < 0.001$, *t* test). n.s., not significant. All values represent mean ± SEM.

VRK3 deletion causes alteration of synaptic protein expression

We next examined the synaptic scaffolds and signaling adaptors/proteins. Among signaling proteins, *VRK3*-KO mice exhibited a marked increase in CaMKIIα and ERK phosphorylation, whereas mTOR and S6K phosphorylation marginally decreased (Fig. 5 A). Among scaffold proteins, there were no differences in the expression levels of Homer1, synaptic GTPase-activating protein (SynGAP), and SAP97 between WT and *VRK3*-KO mice. However, levels of Arc (Sala et al., 2003) were increased, whereas levels of other synaptic proteins, including syntaxin, PAK3, and PSD-95 (Jurado et al., 2013), were reduced (Fig. 5 B). Among the receptor proteins, there were no differences in the expression levels of glutamate receptors (such as mGluR1, GluA2, GluA3, GluN2A, and GluN2B) between WT and *VRK3*-KO mice (Fig. 5 C). Interestingly, GluN1 expression was elevated, whereas TrkB expression was reduced (Fig. 5 C). We further quantified synaptic proteins by separating the synaptosomal PSD fraction. In the total lysate, we found that levels of GluA1, PSD95, and phosphorylated TrkB were decreased. However, the decrease in the GluA1 expression was very subtle, whereas the decrease in levels of both PSD95 and phosphorylated TrkB was obvious in the PSD fraction

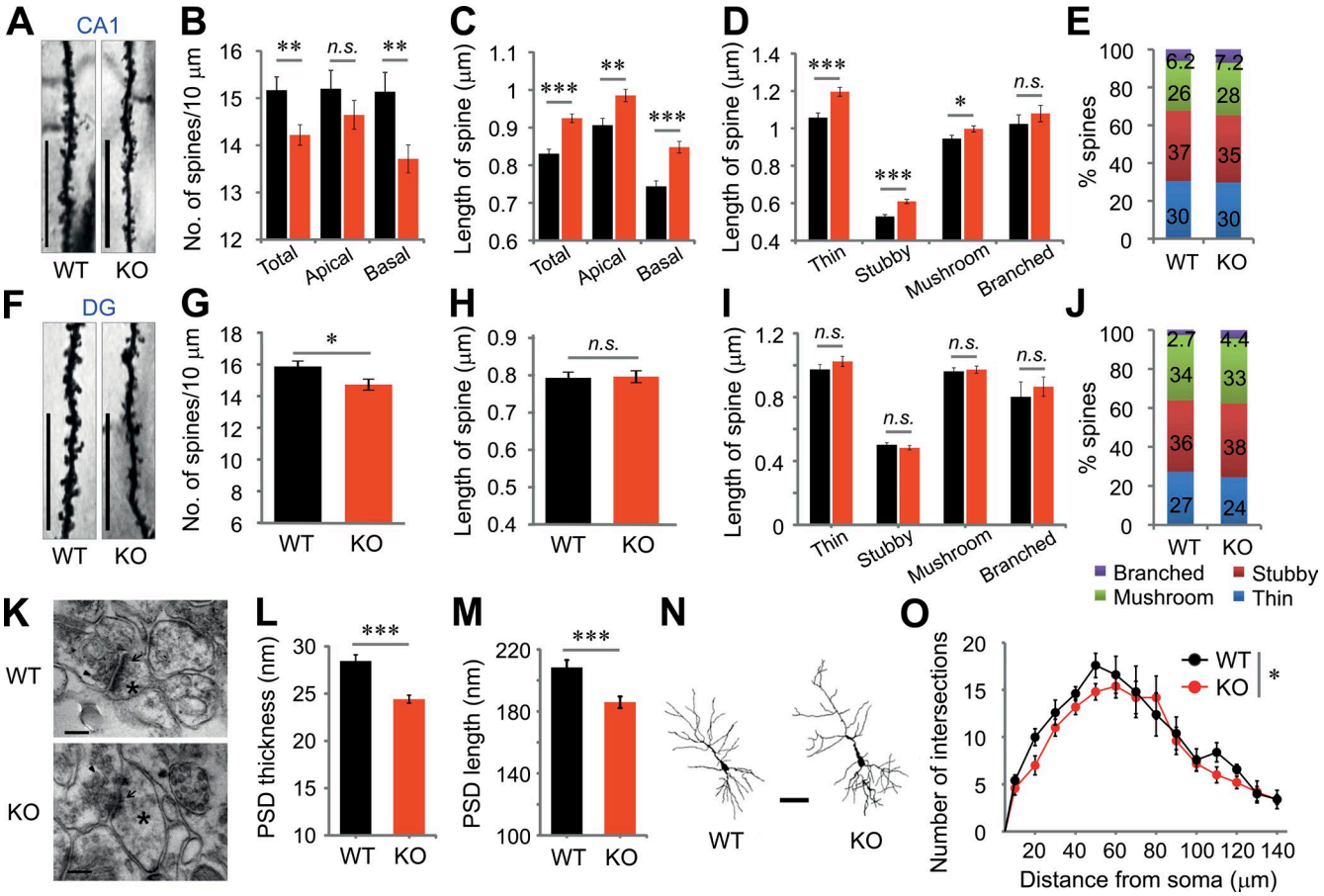

Figure 3. **Alteration of synaptic structures in CA1 and DG regions of *VRK3*-KO mice.** (A) Representative images of dendrites in CA1 pyramidal neurons of WT and *VRK3*-KO mice. Bars, 10 µm. (B) Quantification of spine density (spines per 10 µm) on apical and/or basal dendrites in the CA1 region (n = 44, 114 dendrites from 6, 8 mice of WT and *VRK3*-KO mice, respectively; **, P < 0.01, t test). (C) Quantification of spine length on apical and/or basal dendrites in the CA1 region (n = 665, 1,621 spines from 6, 8 mice; ***, P < 0.001; **, P < 0.01, t test). (D) Dendritic spines in the CA1 region were classified as thin, stubby, mushroom, or branched. Spine length for specific spine subtypes in the CA1 region (n = 88–574 spines from 6, 8 mice; ***, P < 0.001; *, P < 0.05, t test). (E) Comparable proportions of each type of spine on apical and basal dendrites in the CA1 region of WT and *VRK3*-KO mice (n = 6, 8 mice; P > 0.05, χ^2 test). (F) Representative images of dendrites in the DG region of WT and *VRK3*-KO mice. Bars, 10 µm. (G) Quantification of spine density (spines per 10 µm) in the DG region (n = 37, 40 dendrites from four mice per genotype; t_{75} = 2.326, *, P < 0.05, t test). (H) Quantification of spine length in the DG region (P > 0.05, t test). (I) Spine length for specific spine subtypes in the DG region (P > 0.05, t test). (J) Comparable proportions of each type of spine in the DG region of WT and *VRK3*-KO mice (n = 4, 4 mice; P > 0.05, χ^2 test). (K) Representative electron micrographs of hippocampal CA1 synapses showing the presence (magnification 120,000×) of PSD (arrows), synaptic vesicles (arrowheads), and dendritic spines (asterisks). Bars, 200 nm. (L) PSD length (n = 214, 321 synapses from 3, 3 mice; ***, P < 0.001, t test). (M) PSD thickness (n = 155, 236 synapses from 3, 3 mice; ***, P < 0.001, t test). (N) Reconstructions of representative neurons of Golgi-stained pyramidal neurons. Bar, 50 µm. (O) Number of intersections of the dendrite at different distances (radius) from the soma (center of analysis) from Sholl analysis (n = 5 neurons). A repeated-measures ANOVA indicates a statistical significance for genotype ($F_{1,56}$ = 5.63, P = 0.02; *, P < 0.05), but not radius (distance) genotype, interaction ($F_{1,56}$ = 0.61, P = 0.84). n.s., not significant. All values represent mean ± SEM.

(Fig. 5 D). Also, levels of Arc and phosphorylated CaMKIIα were increased in the PSD fraction (Fig. 5 D). We analyzed and compared the PSD fractions in *VRK3*-KO mice at ages 4 and 12 wk but observed no difference in expression patterns between the two groups (Fig. S4). The quantitative ratio of AMPA receptor and NMDA receptor in the PSD fraction was identical in WT and *VRK3*-KO mice (Fig. S4). These data suggest the possibility that expression of the cytoskeleton, scaffolding proteins, and core signaling factors is largely changed in synapses of *VRK3*-KO mice.

Treatment with a TrkB agonist restores a normal expression pattern of the synaptic and signaling proteins altered in *VRK3*-KO mice

Having observed changes in molecular components in *VRK3*-KO mice, we next sought to examine whether restoration of ERK activity can correct the altered expression profile of synaptic proteins. We therefore tested the effect of 7,8-dihydroxyflavone (7,8-DHF), a selective and blood–brain barrier–permeable TrkB agonist, on protein expression in *VRK3*-KO mice. Multiple studies describe the restorable ef-

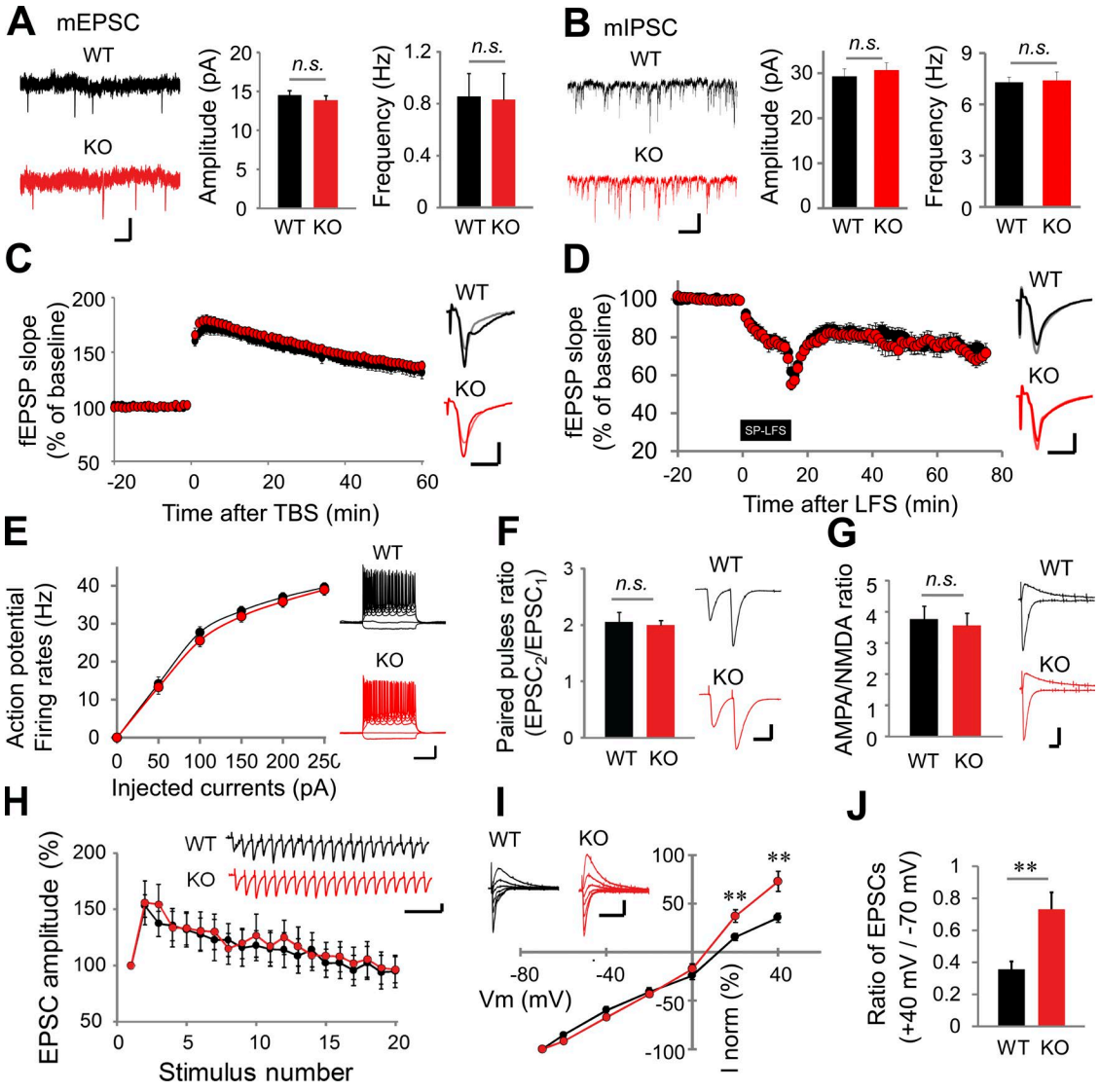

Figure 4. **Altered synaptic transmission in *VRK3*-KO mice.** (A and B) Representative traces, mean amplitude, and frequency of mEPSCs (A; $n = 17, 14$ neurons from 3, 3 mice of WT and *VRK3*-KO mice, respectively; $P > 0.05$, *t* test), and mIPSCs (B; $n = 13, 14$ neurons from 2, 2 mice; $P > 0.05$, *t* test). Bars, 10 pA, 1 s. (C and D) Theta-burst stimulation (TBS)–induced LTP (C; $n = 12, 13$ slices from 4, 4 mice; $P > 0.05$, *t* test.), and single-pulse low-frequency stimulation (SP-LFS)–induced LTD (D; $n = 10, 7$ slices from 4, 4 mice; $P > 0.05$, *t* test) in hippocampal SC-CA1 synapses. Traces were taken 1 min before TBS or SP-LFS (gray, light red) and at the end of the recording period (black, red). Bars, 0.5 mV, 10 ms. (E) Intrinsic excitability measured as firing rates against injected current ($n = 21, 22$ neurons from 3, 3 mice; $P > 0.05$, *t* test) Bars, 20 mV, 0.2 s. (F) Mean paired-pulse ratio (50-ms interstimulus interval) at SC-CA1 synapses ($n = 9, 21$ neurons from 3, 4 mice; $t_{28} = 0.289$, $P > 0.05$, *t* test). Bars, 200 pA, 50 ms. (G) AMPA/NMDA receptor activity ratio ($n = 15, 18$ neurons from 4, 4 mice; $P > 0.05$, *t* test). Bars, 100 pA, 10 ms. (H) 20-Hz stimulation-induced response of hippocampal SC-CA1 synapses ($n = 19, 15$ neurons from 2, 2 mice; $P > 0.05$, *t* test). Bars, 100 pA, 0.2 s. (I) Current-voltage relationship of AMPA receptor/EPSCs after paired conditioning at Vh = −70, −60, −40, −20, 0, 20, and 40 mV ($n = 15, 18$ neurons from 4, 4 mice; **, $P < 0.01$, *t* test). Bars, 100 pA, 0.2 s. (J) The ratio of AMPA receptor/EPSC amplitudes at +40 mV and −70 mV holding is depicted (**, $P < 0.01$, *t* test). n.s., not significant. All values represent mean ± SEM.

fect of 7,8-DHF on synaptic plasticity in a variety of animal models of neurological disorders, including models of Rett's syndrome and fragile X syndrome (Johnson et al., 2012; Tian et al., 2015). First, we confirmed repeatedly that the phosphorylated-ERK/ERK ratio is increased in *VRK3*-KO mice (Fig. 6, A and B). Also, we confirmed that the expression level of TrkB was low in *VRK3*-KO animals (Fig. 6 D). Notably, ERK phosphorylation in WT animals was rapidly increased at 1 h of 7,8-DHF treatment and then returned to base levels, whereas ERK phosphorylation in *VRK3*-KO animals increased in a much slower and delayed manner (Fig. 6 B). Furthermore, an elevated Arc expression in *VRK3*-KO mice returned to a level similar to that in WT mice at 2 h after 7,8-DHF treatment (Fig. 6, A and C). Also, the decreased levels of phosphorylated

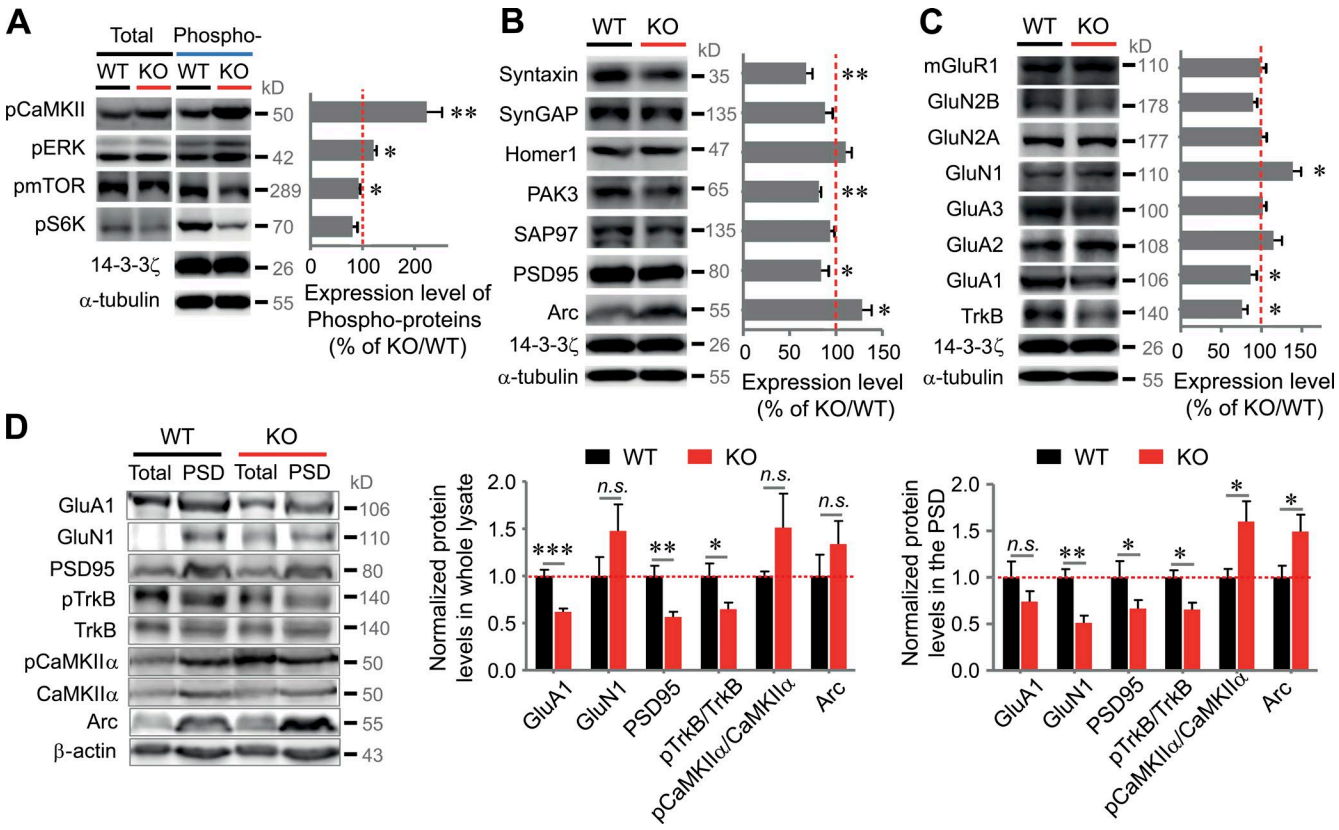

Figure 5. **Biochemical changes in the hippocampal PSD fraction and whole lysates of *VRK3*-KO mice.** (A) CaMKIIα, ERK1/2 (p42/44), mTOR, and S6K proteins. The level of phosphoproteins was normalized by KO/WT ratios of total proteins (n = 5–7 for WT and *VRK3*-KO mice; **, P < 0.01; *, P < 0.05, t test). (B) Levels of syntaxin, SynGAP, Homer1, PAK3, Arc, SAP97, and PSD-95; all proteins were normalized by α-tubulin or/and 14-3-3ζ (n = 5–7 for WT and *VRK3*-KO mice; **, P < 0.01; *, P < 0.05, t test). (C) Levels of mGluR1, GluN1, GluN2A, GluN2B, GluA1, GluA2, GluA3, and TrkB; all proteins were normalized by α-tubulin or/and 14-3-3ζ (n = 5–7 for WT and *VRK3*-KO mice; *, P < 0.05, t test). The same 14-3-3ζ loading control was used in both B and C, being the same test group. (D) Immunoblot analyses of PSD fractions and whole lysates from 12–13-wk old WT and *VRK3*-KO mice for the indicated proteins (left). Protein levels of GluA1, GluN1, PSD-95, phosphorylated TrkB, phosphorylated CaMKIIα, and Arc in the hippocampal whole lysates (middle) and PSD fractions (right) from *VRK3*-KO mice (n = 6 mice per genotype; ***, P < 0.001; **, P < 0.01; *, P < 0.05, t test). β-Actin was used as a loading control, and all values were normalized to the mean level of the respective protein in the PSD fractions or whole lysates from WT mice. n.s., not significant. All values represent mean ± SEM.

TrkB (Fig. 6 D), PSD-95 (Fig. 6 E), phosphorylated mTOR (Fig. 6 F), and phosphorylated S6K (Fig. 6 G) in *VRK3*-KO mice returned to WT levels after 7,8-DHF treatment. These results suggest that aberrant ERK activity induced by *VRK3* deletion caused a marked dysregulation of expression of many synaptic signaling proteins in *VRK3*-KO mice, and a TrkB agonist successfully restored the normal expression profile.

TrkB stimulation recovers altered synaptic structure and function and protein profiles in *VRK3*-KO mice

We reasoned that exogenous application of 7,8-DHF could reverse the abnormal synaptic structure and function and protein profiles of *VRK3*-KO mice. To test the idea, we monitored the effect of 7,8-DHF on synaptic proteins in PSD fractions. Notably, we found that the altered expression of PSD95, phosphorylated TrkB, and GluA1 and GluN1 returned to normal expression level after 7,8-DHF treatment (Fig. 7 A). However, the increased expression of Arc and phosphorylated CaMKIIα in the PSD fraction was not changed by 7,8-DHF treatment (Fig. 7 A). We also found that bath-applied 7,8-DHF successfully reversed the decreased rectification of AMPA receptor–mediated currents in hippocampal slices of *VRK3*-KO mice, whereas 7,8-DHF did not affect AMPA receptor responses in hippocampal slices of WT mice (Fig. 7 B). Finally, we observed that 7,8-DHF restored the reduced number of spines in *VRK3*-KO animals (Fig. 7 C). In particular, 7,8-DHF by itself did not change the number of spines in the apical region of WT animals, implying that 7,8-DHF only suppressed changes caused by VRK3 deficiency.

Acute and chronic TrkB stimulation substantially ameliorates social interaction deficits, but not anxiety, in *VRK3*-KO mice

Finally, we monitored whether 7,8-DHF improves cognitive deficits and autism-like behaviors in *VRK3*-KO mice. To

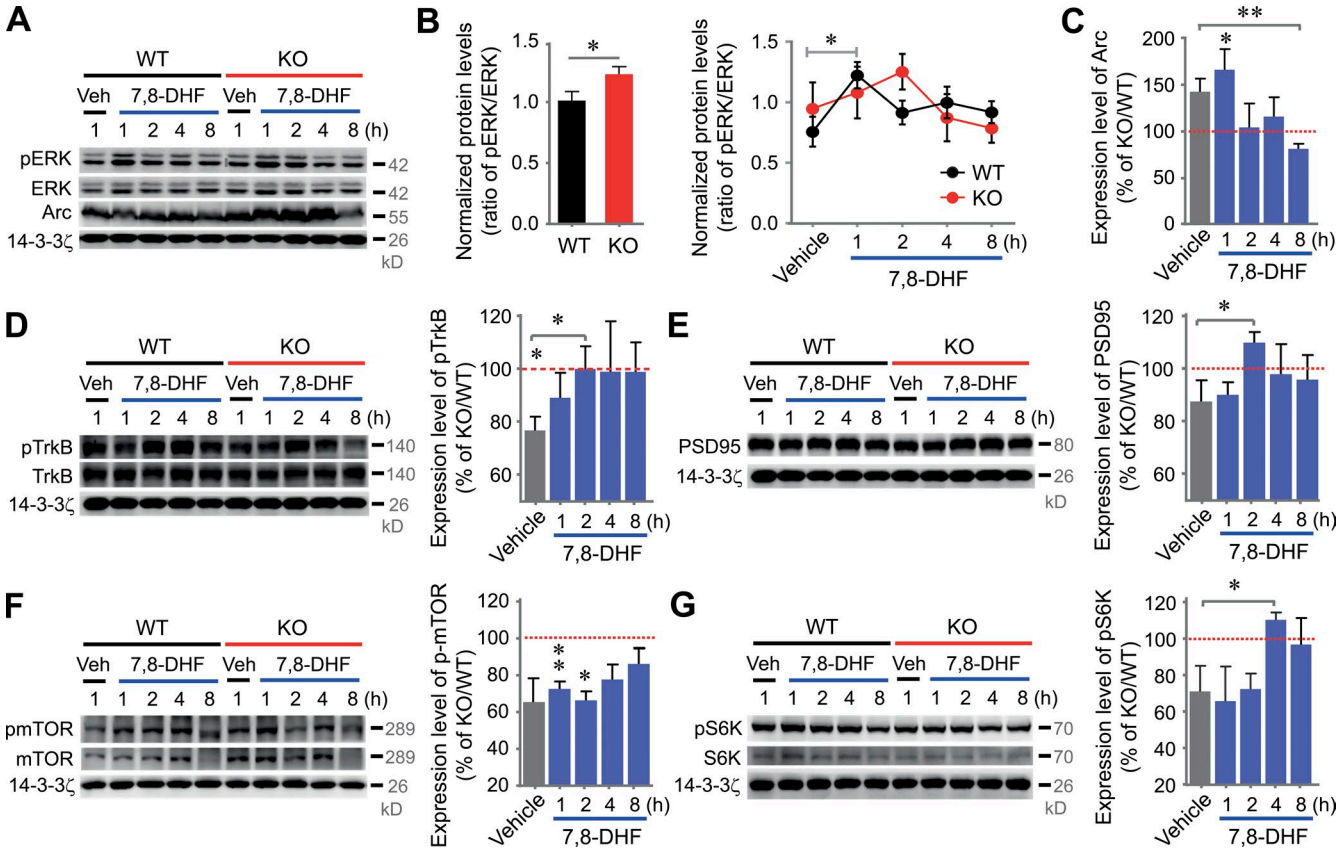

Figure 6. **TrkB stimulation restores dysregulated Arc-induced synaptic plasticity in *VRK3*-KO mice.** (A–C) Representative Western blots (A) and quantitative plots of the time courses of 7,8-DHF–induced ERK (B) and Arc expression (C). Arc protein was normalized by 14-3-3ζ (B: $n = 4/4/4/4/4$ and $n = 4/4/4/4/4$ for vehicle/7,8-DHF(1hr)/7,8-DHF(2hr)/7,8-DHF(4hr)/7,8-DHF(8hr)-treated WT and *VRK3*-KO mice, respectively; *, $P < 0.05$, *t* test; C: $n = 4/4/4/4/4$ for WT and $n = 4/4/4/4/4$ for KO; **, $P < 0.01$; *, $P < 0.05$, *t* test; vehicle-treated *VRK3* KO vs. 7,8-DHF [8 h]–treated *VRK3* KO; **, $P < 0.01$, *t* test). (D–G) Representative Western blots and quantitative plots of the time course of 7,8-DHF–induced TrkB (D), PSD-95 (E), mTOR (F), and S6K (G) activation in *VRK3*-KO mice compared with vehicle-treated WT mice (D: $n = 5/5/5/5/5$ for WT and $n = 5/5/5/5/5$ for KO; WT vs. *VRK3* KO; $t_8 = 2.577$; *, $P < 0.05$, *t* test; vehicle-treated *VRK3* KO vs. 7,8-DHF [2 h]–treated *VRK3* KO $t_8 = 2.325$; *, $P < 0.05$; E: $n = 4/4/4/4/4$ for WT and $n = 4/4/4/4/4$ for KO; $P > 0.05$, *t* test; vehicle-treated *VRK3* KO vs. 7,8-DHF [2 h]–treated *VRK3* KO; *, $P < 0.05$, *t* test; F: $n = 4/4/4/4/4$ for WT and $n = 4/4/4/4/4$ for KO; $P = 0.11$; **, $P < 0.01$; *, $P < 0.05$, *t* test; G: $n = 4/4/4/4/4$ for WT and $n = 4/4/4/4/4$ for KO; $t_6 = 1.538$, $P = 0.17$, *t* test; vehicle-treated *VRK3* KO vs. 7,8-DHF [4 h]–treated *VRK3* KO; *, $P < 0.05$, *t* test). Each densitometry analysis of Western blots in KO mice was normalized by calculation of relative protein levels compared with corresponding values of the vehicle-treated (1 h) and 7,8-DHF–treated (1, 2, 4, and 8 h) WT control group after normalization to 14-3-3ζ levels. The same 14-3-3ζ loading control was used in both D and E, being the same test group. All values represent mean ± SEM.

avoid the possibility of different temporal patterns elicited by the pharmacokinetics of TrkB activation (Ji et al., 2010), we applied acute and chronic modes of 7,8-DHF delivery to the mice. To monitor the acute effect of 7,8-DHF, mice were subjected to behavioral tests at 24 h after three consecutive treatments with 7,8-DHF administered once a day (Fig. 8). In the three-chamber test, 7,8-DHF treatment markedly recovered the impaired social interaction of *VRK3*-KO mice compared with DMSO treatment (Fig. 8, A and B), but the effect was diminished 7 d after treatment (Fig. 8, C and D). We then challenged mice with chronic treatment of 7,8-DHF (from age 4 wk to 11 wk, for a total of 8 wk; Fig. 9). We found that chronic application of 7,8-DHF successfully suppressed the increase in grooming activity (Fig. 9 A) and improved abnormal social activity (Fig. 9, B and C) in *VRK3*-KO mice. Surprisingly, the beneficial effect of 7,8-DHF on social interaction in *VRK3*-KO mice was observed 5 wk after the last injection (Fig. 9 D). The effect of 7,8-DHF on social approach behavior, except for social novelty (Fig. 9, E and G), persisted for up to 13 wk after the last treatment (Fig. 9 F). Finally, we tested the effect of 7,8-DHF on other cognitive changes in *VRK3*-KO mice. We found that acute 3-d consecutive treatments of 7,8-DHF failed to alleviate anxiety behavior in the open field test and EPM (Fig. 10, A and B). Even chronic 7,8-DHF treatment did not affect the increase in anxiety behavior of *VRK3*-KO mice (Fig. 10, C–F). However, in both a passive avoidance test and a novel object recognition test, chronic treatment with 7,8-DHF success-

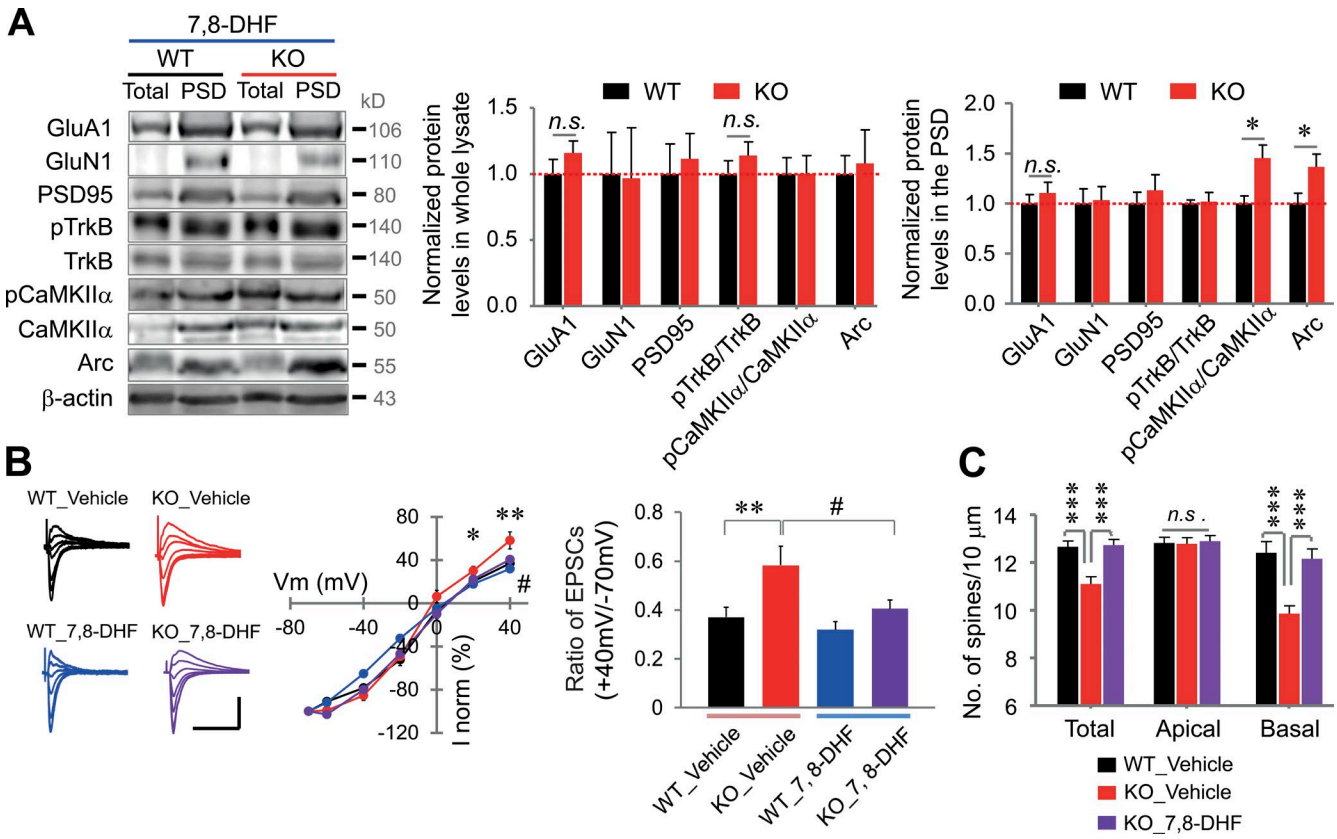

Figure 7. **Improvement of the synaptic changes in *VRK3*-KO mice by TrkB stimulation.** (A) Immunoblot analyses of PSD fractions and whole lysates from mice at 12 wk after final chronic treatment with 7,8-DHF. Protein levels of GluA1, GluN1, PSD-95, phosphorylated TrkB, phosphorylated CaMKIIα, and Arc in the hippocampal whole lysates and PSD fractions (n = 6 mice per genotype; *, $P < 0.05$, t test). β-Actin was used as a loading control, and all values were normalized to the mean level of the respective protein in the PSD fractions or whole lysates from WT mice. (B) Current–voltage relationship of AMPA receptor/EPSCs after paired conditioning at V_h = −70, −60, −40, −20, 0, 20, and 40 mV (middle), and rectification index (right) with or without 7,8-DHF treatment. Bars, 100 pA, 0.2 s. The ratio of AMPA receptor/EPSC amplitudes at +40 mV and −70 mV holding is also depicted (n = 12 neurons from 3 mice for WT_vehicle; n = 13, 3 for *VRK3* KO_vehicle; n = 15, 3 for WT_7,8-DHF; n = 14, 2 for *VRK3* KO_7,8-DHF; **, $P < 0.01$ and *, $P < 0.05$ for WT_vehicle vs. *VRK3* KO_vehicle; #, $P < 0.05$ for *VRK3* KO_vehicle vs. *VRK3* KO_7,8-DHF, two-way ANOVA with Horm-Sidak's post-test). (C) Quantification of spine density (spines per 10 µm) on apical (AC) and/or basal (BS) dendrites in the CA1 region (n = 3 mice per genotype; ***, $P < 0.001$, t test). n.s., not significant. All values represent mean ± SEM.

fully reduced the impairment of learning and/or memory in *VRK3*-KO mice (Fig. S5, A and B). These results clearly show that 7,8-DHF treatment ameliorates not only the impaired social interaction but also stereotyped behaviors and impaired learning and memory in *VRK3*-KO mice and thus support the hypothesis that TrkB stimulation could affect autism-like behaviors in *VRK3*-deficient mice.

DISCUSSION

In this study, we report that *VRK3*-KO mice exhibited the typical symptoms of ASD. *VRK3*-KO animals also showed abnormal synaptic structure and function. These mice showed an altered expression pattern of synaptic and signaling proteins such as aberrant ERK, Arc, and CaMKIIα. Ultimately, we found that long-term stimulation of TrkB by 7,8-DHF treatment markedly reversed autism-like behavior in *VRK3*-KO mice. Thus, we provide compelling evidence that *VRK3* plays essential roles in synaptic structure and function, which eventually modulate a series of cognitive functions. In addition, our results strongly suggest that *VRK3*-KO mice represent an animal model of ASD and that TrkB activation can be a possible therapeutic approach to *VRK3*-related ASD.

A recent study suggests that de novo CNVs are predominant causes of ASD, although the genetic etiology of ∼70% of forms of ASD is unknown (Ebert and Greenberg, 2013). From the DECIPHER database and AutismKB database, we identified CNVs encompassing 19:50086504-52125032 (interval 2.04Mb) and 19:54013696-55502526 (AutismKB database–reported CNV ID AutCNV0000648), respectively, at the 19q13.33 region, which includes the *VRK3* gene, that are associated with ASD and intellectual disability (DECIPHER-reported patient ID 251777; Firth et al., 2009; Xu et al., 2012). Haploinsufficiency, wherein a single functional copy of a gene is insufficient to maintain normal function, is a major cause

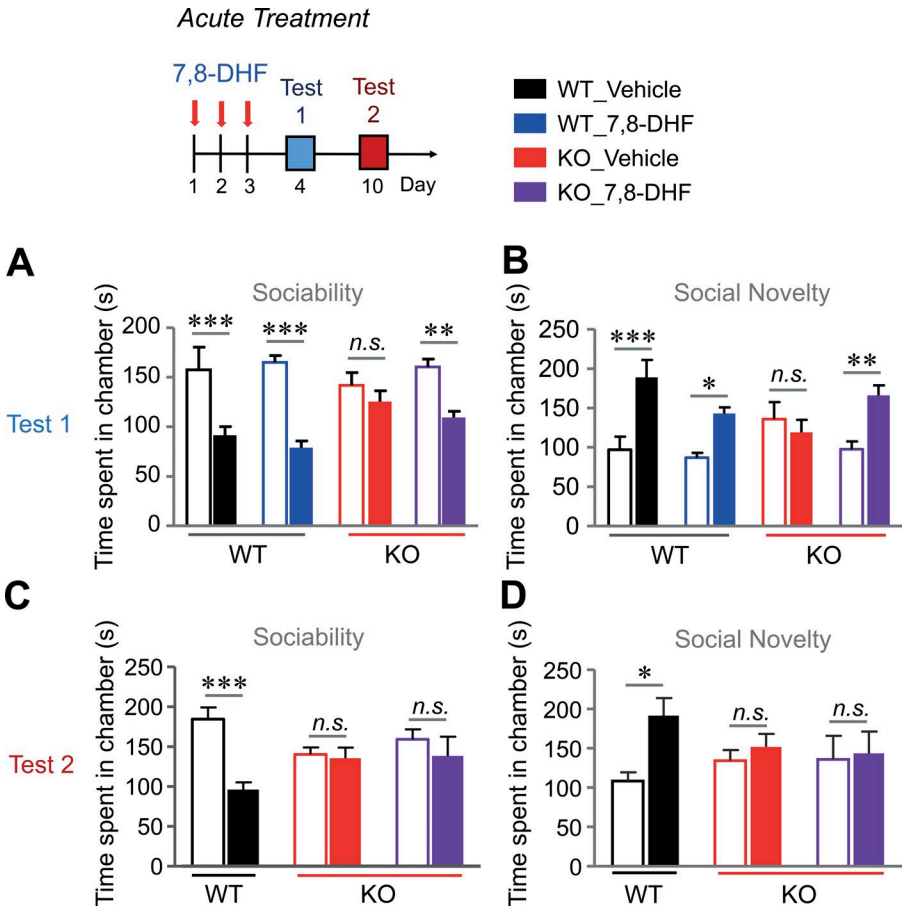

Figure 8. **Recovery of social interaction deficits by acute treatment with 7,8-DHF in *VRK3*-KO mice.** (A and B) Sociability and preference for social novelty at 1 d (test 1) after acute treatment with 7,8-DHF or vehicle; sociability with mouse 1 (blank bar) versus object (filled bar; A: n = 7, 8 and 8, 9 for WT and *VRK3*-KO mice; WT vs. *VRK3* KO $F_{1,56}$ = 49.99, P < 0.0001, interaction $F_{3,56}$ = 3.61, P = 0.0186, two-way ANOVA; ***, P < 0.001; **, P < 0.01; Bonferroni's post-test) and preference for social novelty with familiar mouse (blank bar) versus novel mouse (filled bar; B: WT vs. *VRK3* KO $F_{1,56}$ = 22.17, P < 0.0001, interaction $F_{3,56}$ = 4.58, P = 0.0069, two-way ANOVA; ***, P < 0.001; **, P < 0.01; *, P < 0.05; Bonferroni's post-test). (C and D) Sociability and preference for social novelty at 7 d (test 2) after acute treatment with 7,8-DHF or vehicle, sociability (C: n = 7 and 8, 9 for WT and *VRK3*-KO mice; WT vs. *VRK3* KO $F_{1,42}$ = 10.01, P = 0.0029, interaction $F_{2,42}$ = 4.55, P = 0.0163, two-way ANOVA; ***, P < 0.001, Bonferroni's post-test), and preference for social novelty (D: WT vs. *VRK3* KO $F_{1,42}$= 4.13, P = 0.0487, two-way ANOVA; *, P < 0.05, Bonferroni's post-test). n.s., not significant. All values represent mean ± SEM.

of developmental diseases (Huang et al., 2010). Hence, taking into account that 78.63% and 88.9% of haploinsufficiency reported in the DECIPHER database and UCSC Genome Browser, respectively, are expected mutations or deletions of *VRK3*, we can surmise that *VRK3* deletion may also constitute one cause of ASD. We found that *VRK3*-KO animals show a series of cognitive impairments that are frequently monitored in human ASD patients. *VRK3*-KO animals displayed autism-like behaviors, including hyperactivity, stereotyped behaviors, and reduced social interaction, as well as impaired context-dependent spatial memory. We also found that *VRK3*-heterozygote mice exhibit behaviors similar to those of *VRK3*-KO animals. These findings support a model in which *VRK3* gene haploinsufficiency leads to aberrations in neuronal functioning, resulting in impaired cognitive and behavioral abnormalities.

Because synaptic dysfunction is an important pathological mechanism in ASD (Delorme et al., 2013; Sztainberg and Zoghbi, 2016), we further characterized the synaptopathy in *VRK3*-KO animals. The structural stability of synaptic spine is very important for neuronal functions (Lin and Koleske, 2010; Caroni et al., 2012) and is one pathological mechanism in ASD (Hullinger et al., 2016; Lin et al., 2016). Our results show structural defects of *VRK3*-KO mice, along with a decrease in spine number (Fig. 3 B) and dendritic arborization (Fig. 3 O). Electronic microscopy results clearly showed a decreased length and thickness of the PSD structure (Fig. 3, L and M). These results lead us to conclude that the loss of function of *VRK3* results in a synaptic structural defect. The physiological characteristics are largely normal in *VRK3*-KO synapses, so we assume two reasons for this defect: (1) relatively weak changes in signaling factors that fail to produce profound functional changes, and (2) compensation mechanisms, possibly from changes in binding partners, another subtype, or down-stream signal transduction. A clearer understanding of the physiological compensation mechanism observed in our VRK3-KO animals requires further study. Interestingly, *VRK3*-KO animals showed decreased rectification of AMPA receptor–mediated postsynaptic currents, which is mediated by altered AMPA receptor composition and a decrease in GluA2-lacking Ca^{2+}-permeable AMPA receptors (Anggono and Huganir, 2012). In fact, the modulation of Ca^{2+}-permeable AMPA receptors caused by changes in AMPA receptor composition regulates neuronal function, and its perturbation causes neurological disease (Liu and Zukin, 2007; Clem and Huganir, 2010; Whitehead et al., 2017). Thus, our results provide an important clue about the relationship between ASD-related behavior and Ca^{2+}-permeable AMPA

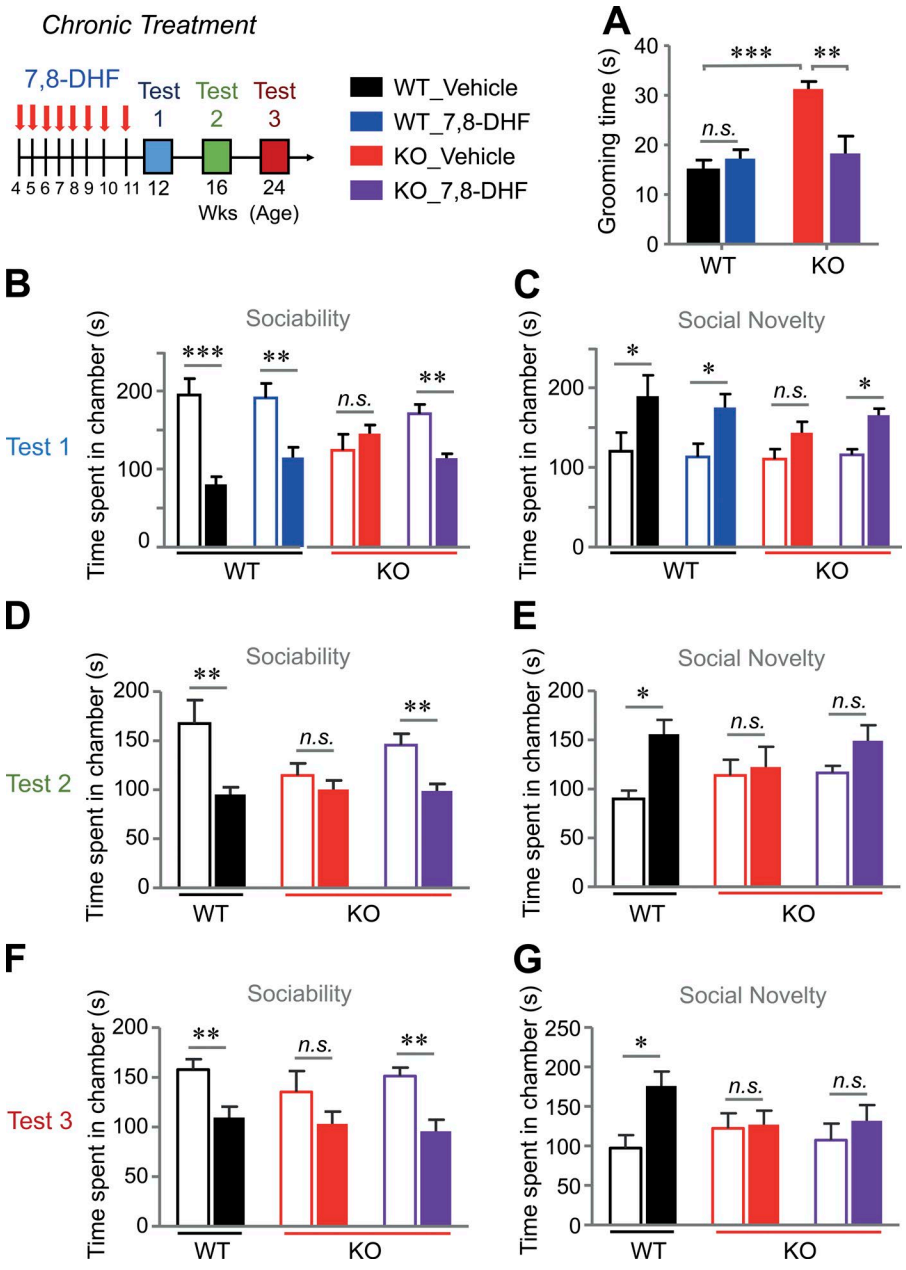

Figure 9. **Recovery of social interaction deficits and stereotyped behaviors by chronic treatment with 7,8-DHF in *VRK3*-KO mice.** (A) Duration of grooming behavior 1 wk (test 1) after final chronic treatment with 7,8-DHF or vehicle in WT and *VRK3*-KO mice (n = 5–7 for WT and *VRK3*-KO mice; ***, P < 0.001; **, P < 0.01; t test). (B and C) Sociability and preference for social novelty at 1 wk (test 1) after final chronic treatment with 7,8-DHF or vehicle, sociability with mouse 1 (blank bar) versus object (filled bar; B: n = 6, 7 and 6, 9 for WT and *VRK3*-KO mice; WT vs. *VRK3* KO $F_{1,48}$ = 31.50, P < 0.0001, interaction $F_{3,48}$ = 7.17, P = 0.0005, two-way ANOVA; ***, P < 0.001; **, P < 0.01, Bonferroni's post-test), and preference for social novelty with familiar mouse (blank bar) versus novel mouse (filled bar; C: n = 6, 7 and 6, 9 for WT and *VRK3*-KO mice; WT vs. *VRK3* KO $F_{1,48}$ = 25.13, P < 0.0001, two-way ANOVA; *, P < 0.05, Bonferroni's post-test). (D and E) Sociability and preference for social novelty at 5 wk (test 2) after final chronic treatment with 7,8-DHF or vehicle, sociability (D: n = 5 and 6, 8 for WT and *VRK3*-KO mice; WT vs. *VRK3* KO $F_{1,32}$= 16.84, P = 0.0003, two-way ANOVA; **, P < 0.01; Bonferroni's post-test), and preference for social novelty (E: n = 5 and 6, 8 for WT and *VRK3*-KO mice; WT vs. *VRK3* KO $F_{1,32}$= 8.89, P = 0.0055, two-way ANOVA; *, P < 0.05, Bonferroni's post-test). (F and G) Sociability and preference for social novelty at 13 wk (Test 3) after final chronic treatment with 7,8-DHF or vehicle; sociability (F: n = 5 and 6, 8 for WT and *VRK3*-KO mice; WT vs. *VRK3* KO $F_{1,32}$= 20.13, P < 0.0001, two-way ANOVA; **, P < 0.01; Bonferroni's post-test), and preference for social novelty (G: n = 5 and 6, 8 for WT and *VRK3*-KO mice; WT vs. *VRK3* KO $F_{1,32}$= 5.04, P = 0.0315, two-way ANOVA; *, P < 0.05, Bonferroni's post-test). n.s., not significant. All values represent mean ± SEM.

receptors, offering a motivation to monitor the changes in Ca^{2+}-permeable AMPA receptors in other animal models of ASD-related behavior.

We previously studied the mechanisms of *VRK3* action and found that *VRK3* is a negative modulator of ERK that affects many signaling pathways (Kang and Kim, 2006). Because ERK has various effects on synaptic proteins as well (Chao, 2003; Santos et al., 2010), the expression of signaling molecules, scaffolding proteins, and receptors in relation to synaptic proteins are likely altered in *VRK3*-KO mice. In our results, ERK phosphorylation in *VRK3*-KO animals increased in a much slower and delayed manner compared with WT animals, which showed much faster kinetics of ERK phosphorylation (Fig. 6 B). We hypothesized that this was because (1) the basal level of phosphorylated ERK was already increased in *VRK3*-KO mice, and (2) a lower level of TrkB expression in *VRK3*-KO mice caused slow additional activation of ERK. It has been suggested that TrkB signaling is also a critical pathway modulating changes in synaptic strength for cognitive processes such as memory formation (von Bohlen und Halbach et al., 2006; Minichiello, 2009; Fortin et al., 2012; Bennett and Lagopoulos, 2014). In our results, it is important to note that the difference between ERK phosphorylation in both WT and *VRK3*-KO mice was decreased when 7,8-DHF treatment was sustained (e.g., in 4–8 h), despite the different time course/kinetics of the 7,8-DHF ef-

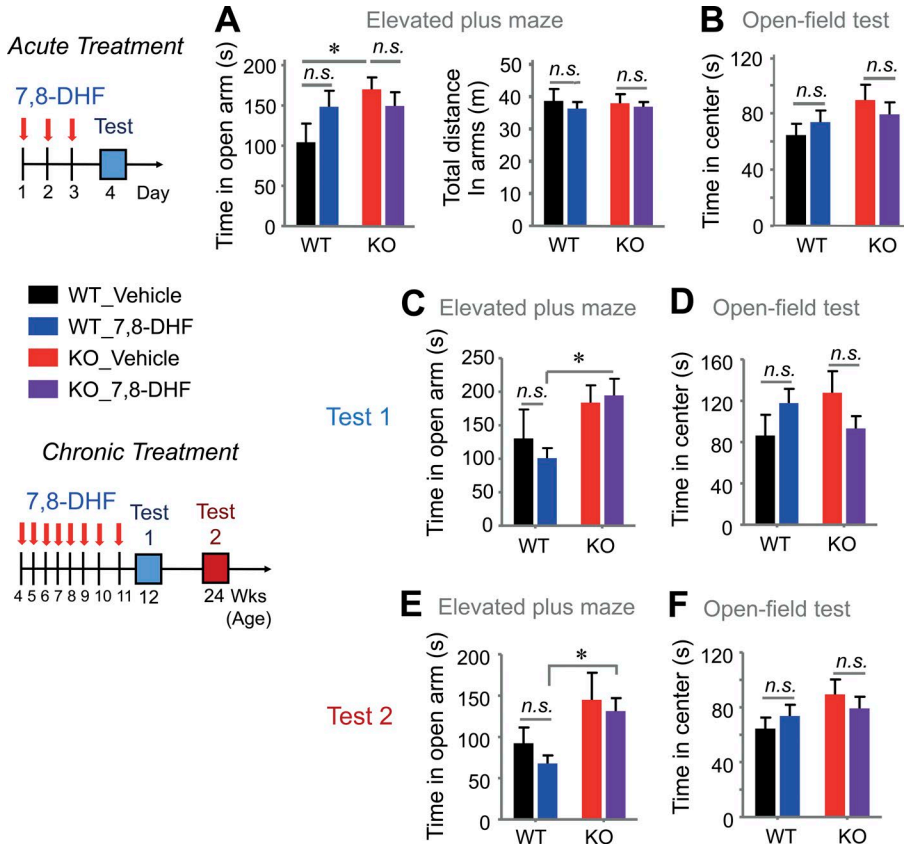

Figure 10. **Acute and chronic TrkB stimulation have no effect on anxiety in *VRK3*-KO mice.** (A) Duration of time spent (left) and total locomotor activity (right) in the open arms of the elevated plus maze 1 d (test) after acute 7,8-DHF or vehicle treatment in WT and *VRK3*-KO mice (n = 6, 6 and 7, 10 for WT and *VRK3*-KO mice). (B) Locomotor activity in the center region of the open field as shown by time spent in the center 1 d (test) after acute 7,8-DHF or vehicle treatment (n = 7, 8 and 8, 10 for WT and *VRK3*-KO mice). Chronic treatment with 7,8-DHF and test schemes. (C and D) Duration of time spent in the open arms of the elevated plus maze (C) and in the center region of the open field (D) at 1 wk (test 1) after final chronic treatment with 7,8-DHF or vehicle (n = 5–8 for WT and *VRK3*-KO mice). (E and F) Duration of time spent in the open arms of the elevated plus maze (E) and in the center region of the open field (F) at 13 wk (test 2) after chronic treatment with 7,8-DHF or vehicle (n = 6–10 for WT and *VRK3*-KO mice). n.s., not significant. *, $P < 0.05$, two-tailed t test. All values represent mean ± SEM.

fect. The phenotypes in *VRK3*-KO mice are likely mediated by ERK, as *VRK3* interacts with ERK and negatively modulates ERK phosphorylation. Therefore, we hypothesize that changes in signaling factors such as Arc, phosphorylated TrkB, PSD-95, phosphorylated mTOR, and phosphorylated S6K in *VRK3*-KO mice are caused by basally increased ERK activation. We confirmed that the difference in these signaling factors between *VRK3*-KO and WT mice was also reduced when 7,8-DHF treatment was sustained. CaMKIIα is also a major variable in *VRK3*-KO mice and an important modulator of synaptic structure and function. However, we found that 7,8-DHF failed to reverse the increase in phosphorylated CaMKIIα in the PSD fraction of *VRK3*-KO mice to WT levels, whereas reduced levels of PSD95 and phosphorylated TrkB were significantly restored by 7,8-DHF treatment (Fig. 7 A). These results lead us to confirm that 7,8-DHF treatment restores the structural and functional phenotypes in *VRK3*-KO mice via an ERK-dependent signaling pathway.

For an in-depth look at the etiological mechanisms of autism-like behavior in *VRK3*-KO mice, it is important to compare the characteristics of *VRK3*-KO mice with those of existing ASD animal models. Ube3a knockout is a well-known animal model of Angelman syndrome, and these mice exhibit autism-like behavior. Interestingly, some phenomena we observed in *VRK3*-KO mice are similar to those observed in Ube3A-KO animals (e.g., analogous up-regulation of CaMKIIα and Arc and down-regulation of PSD-95, mTOR, GluA1, and TrkB; Weeber et al., 2003; van Woerden et al., 2007; Cao et al., 2013; Ebert and Greenberg, 2013). An increase in Arc levels in the Ube3a-KO mouse is a phenotype that also appears in the *VRK3*-KO mouse. However, Ube3a maternal-deficient mutant animals show a decreased LTP (Weeber et al., 2003), whereas *VRK3*-KO animals show an intact LTP. In addition, Ube3a-KO animals have normal phosphorylated ERK levels, whereas *VRK3*-KO animals have increased phosphorylated ERK levels (Cao et al., 2013). In fact, the various characteristics of the ASD animal models make it difficult to define the etiological mechanism of ASD as a single factor/pathway. For example, NMDA receptor activity, the most widely recognized ASD-related factor to date, varies widely among ASD animal models (Lee et al., 2015; Kim et al., 2017). Because ERK is one of the downstream signals of NMDA receptor signaling (Thomas and Huganir, 2004), it is also closely related to our *VRK3*-KO study. However, Ube3a-KO animals (Yashiro et al., 2009; Kaphzan et al., 2012) and our *VRK3*-KO animals (Fig. 4 G) commonly have a normal NMDA/AMPA ratio, whereas neurologin-1–KO animals (Blundell et al., 2010), Shank2-KO animals (Won et al., 2012), and Shank3-KO animals (Peça et al., 2011) show reduced NMDA functioning, including a reduced NMDA/AMPA ratio. Even IRSp53-KO mice with autism-like behavior exhibit increased NMDA

functioning (Chung et al., 2015). These findings suggest that the etiology of ASD cannot be elucidated with a single causal factor. For that reason, it may be difficult to treat patients with mutations in Ube3a in the same way as patients with neuroligin-1 mutations, suggesting that appropriate treatment can be provided by accurately assessing the cause of ASD in individual patients. Therefore, we expect that efforts to identify and analyze ASD-related factors such as *VRK3* will become increasingly important in the future.

Many studies have focused on applying exogenous BDNF to the brainstem preparation and found that it corrected synaptic defects and neuronal dysfunction (Lu et al., 2013). However, because of the difficulty in central nervous system delivery and the poor bioavailability of BDNF, 7,8-DHF, which imitates BDNF and acts as a robust TrkB agonist, has been proposed as a potential therapeutic tool (Lu et al., 2013). Using a combination of in vivo and in vitro application of 7,8-DHF, we have found that acute and chronic TrkB activation by 7,8-DHF has beneficial effects on autism-like behaviors of *VRK3*-KO mice. Intriguingly, the acute application of 7,8-DHF in adult mice elicited a short-lasting effect, but long-term stimulation of TrkB by 7,8-DHF treatment in younger mice almost completely recovered the impairment of social interaction in *VRK3*-KO mice. In addition, long-term treatment with 7,8-DHF restored stereotyped behaviors and impaired learning and/or memory in *VRK3*-KO mice. It has been widely considered that developmental alterations of neuronal networks may be difficult to restore by pharmacological intervention after the expected onset of symptoms. Therefore, our results demonstrate that long-term stimulation of TrkB before the onset of ASD symptoms is an effective strategy for the treatment of neurodevelopmental disorders. Finally, 7,8-DHF treatment failed to significantly affect anxiety in *VRK3*-KO mice (Fig. 10). The hypothesis that ASD and anxiety are consistently correlated is somewhat controversial, although it is generally assumed that ASD is linked to increased anxiety. For example, like *VRK3*-KO mice, MeCP2-KO and Cdkl5-KO mice exhibit reduced anxiety with autism-like behavior (Pelka et al., 2006; Chahrour and Zoghbi, 2007; Wang et al., 2012). Our results suggest that autism-like behavior and anxiolytic behavior in *VRK3*-KO mice occur through different mechanisms.

Collectively, the key finding of the current study is that *VRK3* deletion can cause down-regulation of TrkB and evoke abnormal spine and PSD structure and synaptic dysfunction, which lead to cognitive impairment and ASD-related behaviors that are caused by chromosomal abnormalities. We have also found that chronic TrkB activation by 7,8-DHF treatment rescues impaired social interaction and learning/memory in *VRK3*-KO mice, which supports the hypothesis that TrkB stimulation could ameliorate autism-like behavior in *VRK3*-deficient mice. Our work is the first to validate that reduced *VRK3* expression affects synaptic and cognitive function and suggests that TrkB stimulation is a possible pharmacotherapeutic strategy for the treatment of *VRK3*-related ASD.

MATERIALS AND METHODS

Generation of *VRK3*-KO mice

The gene-trapped embryonic stem cell line YTA189 (http://www.informatics.jax.org/allele/MGI:3880442) was obtained from BayGenomics (Stryke et al., 2003). This cell line was generated using a gene trap protocol with the pGT0Lxf construct, which contains the intron from engrailed 2 upstream of a gene encoding β-galactosidase/neomycin resistance, β-geo (http://www.genetrap.org). The embryonic stem cell clone was injected into a C57BL/6 blastocyst according to standard procedures (Stryke et al., 2003; Bult et al., 2010). Male chimeras were bred with C57BL/6 mice to create animals with a germline transmission of the mutant allele. Heterozygous mice were backcrossed with C57BL/6 mice for a minimum of six generations before the study. Genotyping was performed by PCR and Southern blot using DNA extracted from mouse tails. Insertion of the neomycin phosphotransferase cassette was verified by PCR (neomycin primer: sense, 5′-GTTCTTTTTGTCAAGACCGACCT-3′; antisense, 5′-CTCTTCAGCAATATCACGGGTAG-3′; Int7 primer: sense, 5′-TTTATGAAGTGACCAAAGACCTGA-3′; antisense, 5′-GGGCTAGCATCTCAACTACTACCT-3′).

Quantitative real-time RT-PCR

Total cerebral RNA was isolated and purified with TRI reagent (Molecular Research Center) from 12-wk-old WT or *VRK3*-KO littermate mice. Isolated RNA was reverse transcribed using the ImProm-IITM Reverse Transcription System (Promega) according to the manufacturer's instructions. For detection and quantification, the StepOnePlus Real-Time PCR System (Applied Biosystems) was used. The sequences of the forward and reverse primers were as follows: mouse *VRK3*, 5′-TGGGCTATGGCTTCACCTAC-3′ and 5′-GGACCCATAAAGCCACTTGA-3′; mouse ribosomal protein L32 (Rpl32), 5′-AACCCAGAGGCATTGACAAC-3′ and 5′-CACCTCCAGCTCCTTGACAT-3′.

Behavioral analysis

All procedures for animal experiments were performed in accordance with Pohang University of Science and Technology guidelines on animal care and use and were approved by Pohang University of Science and Technology Institutional Animal Care and Use Committee (approval no. 2013–03-003-R1). Mice were fed ad libitum, and two to four animals were housed in a cage under a 12-h light cycle. Male mice were used for behavioral experiments and nonbehavioral experiments, which mainly were performed with age-matched littermate pairs of male mice younger than 4 wk. All behavioral tests were conducted and analyzed by an experimenter blind to the genotype of the mice. All behavioral assessments were conducted when mice were 12–15 wk old. All experiments were conducted during the light cycle and included littermate controls. Mice that showed poor health (e.g., skin lesions and slowed movement) or failed behavioral experiments (e.g., a fall from the platform of the Barnes circular maze) were excluded from behavioral testing.

Passive avoidance

Long-term memory was assessed with a step-through passive avoidance box (LETICA LE 872; Bioseb) divided into a wide, white, illuminated compartment (250 W × 250 D × 240 H cm^3) and a small, black, dark compartment (195 W × 108 D × 120 H cm^3). Mice were detected by a weight sensor under the floor covering both compartments. The grid of the dark compartment was designed to deliver an electric foot shock. For acquisition and conditioning, a mouse was placed in the illuminated compartment and allowed to freely explore the compartment until entering dark compartment. Each trial occurred as follows: the mouse was placed in the illuminated compartment at the furthest place from the closed door. After 10 s, the door opened. As soon as the mouse entered the dark compartment (the step-through maximum latency was fixed at 50 s, and all mice entered the dark compartment), the door was closed, and after 2 min, the mouse received a single inescapable electric shock (0.3 mA, 1 s). The mouse then remained in the dark chamber for an additional 20 s before being removed and returned to its home cage. Two days later, the mouse was tested for memory retention. The mouse was returned to the white compartment (closed door for 10 s), and the latency to enter the dark compartment was recorded. The maximum step-through latency was 600 s, and this value was recorded if the mouse did not enter the dark compartment. No electric shock was given during this session. All data are shown as mean ± SEM and analyzed using two-way ANOVA with Bonferroni's post hoc analysis.

Novel object recognition

The novel object recognition test was performed in an open field apparatus. During the habituation phase, a mouse was placed in the open field arena and allowed to explore for 10 min of habituation without any objects for 3 d. After habituation, two objects of similar size, shape, and color were placed in opposite corners of the arena, 10 cm from the side walls, and the mouse was placed in the center of the arena and allowed to explore the arena and two objects for 10 min. After 24 h, during the test phase, one object was replaced with a novel object that was of similar size but different shape and color. Then, the mouse was placed in the center and allowed to explore the arena and the two objects. Mouse movements were tracked and recorded by real-time video-tracking computer software Smart Version 2.5 (Panlab) linked to an overhead video camera. The time spent in each chamber and exploratory activity around the objects (2.5-cm zone around the objects) was recorded by real-time video-tracking computer software Smart Version 3.0 (Panlab) and video recording system (DT acquire software/Ancamcorder 3.3.4; Antools) and analyzed by two human observers blinded to genotype and not related to this experiment. All data are shown as mean ± SEM and analyzed using two-way ANOVA with Bonferroni's post hoc analysis.

Barnes circular maze

The test was performed as described previously (Han et al., 2012), with minor modifications. The Barnes circular maze consisted of a circular planar white Plexiglas platform (92-cm diameter) elevated 1 m from the floor with 20 evenly spaced holes (7-cm diameter) located 5 cm from the perimeter. A black escape box (15 × 7 × 7 cm) was placed under one hole. Spatial cues with distinct patterns and shapes were placed on the wall of the testing room. A 500-lux light was turned on during the trial. An experimenter was positioned in the same place with minimal movements throughout the trials. The platform and escape box were cleaned thoroughly with 70% ethanol and paper towels between each trial to remove olfactory cues. 1 d before the training trials began, test mice were habituated in the target box for 3 min. The training trials were repeated for four consecutive days, and three trials were performed each day with 20-min intertrial intervals. At the beginning of each trial, a mouse was placed in the cylindrical holding chamber (10-cm diameter) located in the center of the maze. After 10 s of holding time, the mouse was allowed to search for the target hole for 3 min. If the mouse failed to find the target hole in 3 min, it was gently guided into the target hole by the experimenter's hands. When the mouse entered the escape box, the light was turned off, and the mouse remained undisturbed for 1 min. During training, the movement of the mouse was recorded and the number of errors and latency to find the target hole was measured by real-time video-tracking computer software Smart Version 2.5 linked to an overhead video camera. On days 5 and 12, a probe trial was performed. The escape box was removed during the probe trials, and the mouse was allowed 90 s to find the target hole. During the probe trial, total distance moved and latency to find the target hole were measured. The percentages of correct pokes and time in the target area were also analyzed by real-time video-tracking computer software (Smart Version 2.5). All data are shown as mean ± SEM and analyzed using two-way ANOVA with Bonferroni's post-hoc analysis.

Stereotyped behavior

The time mice spent grooming during a 10-min open field test period was measured. Grooming behavior was defined as scratching or stroking of the face, head, or body with the two forelimbs or licking body parts. The observer was blind to mouse genotype. All data are shown as mean ± SEM and analyzed using Student's two-tailed, unpaired *t* tests.

Three-chamber test

The test was performed as described previously (Nadler et al., 2004; Silverman et al., 2010), with minor modifications. The three-chamber apparatus was a transparent Plexiglas box (60 W × 45 D × 40 H cm^3) with two transparent partitions dividing left, center, and right chambers (20 × 45 cm). Each partition had a square opening (10 × 10 cm) in the bottom center. A cylindrical wire cage (8.5-cm diameter) was used as an inanimate object. A cylindrical bottle filled with water

was placed on the top of the wire cup to prevent the mouse from climbing to the top of the cup. The three-chamber unit and wire cups were cleaned with 70% ethanol and wiped with paper towels between each trial. The three-chamber test consisted of three phases. In the first phase, for habituation, a test mouse was placed in the center of the three-chamber unit and allowed to explore the environment for 10 min. After habituation, an age- and gender-matched same strain mouse that had never been exposed to the test mouse (M1) was placed in one of the two wire cages. The empty wire cage as an inanimate object (O) cue was placed on the other side. Then, the test mouse was placed in the center and allowed to freely explore the chamber for 10 min. In the third phase, a second age- and gender-matched C57BL/6J mouse (M2) that had never been exposed to the test mouse was placed in the previously empty wire cage. Thus, the test mouse would have the choice between a mouse that was already familiar (M1) and a novel mouse (M2). The test mouse was placed in the center and allowed to freely explore the chamber for 10 min. Exploration was defined as each instance in which the test mouse sniffed the empty cage/mouse or oriented its nose toward and came close to the object/stranger. The movement of the mouse was tracked and recorded by real-time video-tracking computer software (Smart Version 2.5) linked to an overhead video camera. Time spent in each chamber and in a circular area (5-cm radius) around each wire cage was analyzed by real-time video-tracking computer software (Smart Version 2.5). All data are shown as mean ± SEM and analyzed using two-way ANOVA with Bonferroni's post hoc analysis.

Pup retrieval

Virgin female mice were isolated for 4 d before the pup retrieval test. Three pups (1–3 days old; C57BL/6) were placed in three different corners of the home cage of the mouse. Mice were allowed to retrieve the pups for 10 min. If mice did not complete retrieval within 10 min, the test was terminated. The movement of mice was observed via an overhead video camera linked to a monitor with Smart Version 2.5. The latencies of pup retrieval were recorded. All data are shown as mean ± SEM and analyzed using two-tailed, unpaired Student's *t* tests or two-way ANOVA with Bonferroni's post hoc analysis.

Nesting behavior

Isolated mice were given nest-building material, a white folded Kimwipe, in the center of their home cages. After 1, 2, and 3 d, the nesting material was photographed. Nesting was scored on a scale of 0 to 3 based on the extent to which the nesting material was converted into fine pieces. All data are shown as mean ± SEM and analyzed using two-way ANOVA with Bonferroni's post hoc analysis.

Open field test

Spontaneous exploratory activity and anxiety-like behavior were assessed in an automated open field. The open field test was performed as previously described (Chao et al., 2010). In brief, mice were placed in a wooden box (60 W × 40 D × 20 H cm^3), and mouse movements were recorded and analyzed by real-time video-tracking computer software (Smart Version 2.5) linked to an overhead video camera. The total distance traveled and time spent in the center (20 × 20–cm imaginary square) were measured for 10 min. The open field arena was cleaned with 70% ethanol and wiped with paper towels after each trial. All data are shown as mean ± SEM and analyzed using two-tailed, unpaired Student's *t* tests.

EPM

The EPM apparatus was a plus-shaped maze elevated 60 cm above the floor. It consisted of two closed arms surrounded by 30-cm-high opaque walls and two open arms (110 × 110 cm). Each mouse was placed in the center (5 × 5 cm) of the maze facing one of the closed arms and allowed to explore the space for 15 min. The movement of mice was tracked and recorded via an overhead video camera and further analyzed by real-time video-tracking computer software (Smart Version 2.5). Time spent in the closed arms, center, and open arms was measured. The maze was cleaned with 70% ethanol and wiped with paper towels between each trial. All data are shown as mean ± SEM and analyzed using two-tailed, unpaired Student's *t* tests.

Light–dark exploration

The light–dark test is based on the natural conflict of mice between an innate aversion to brightly illuminated areas and the desire to explore a novel environment. The apparatus consisted of a light compartment made of white plastic (20 × 20 × 20 cm^3) and a dark compartment made of black plastic (20 × 20 × 20 cm^3). The light and dark compartments were separated by a partition with a tunnel (13× 7.5 × 13.5 cm^3) to allow passage from one compartment to the other. The light compartment was brightly illuminated with a light intensity of 400 lux, and the dark compartment was black-walled and covered at the top with black Plexiglas. At the beginning of the test, a mouse was placed in the center of the light compartment facing the tunnel, and the door of the tunnel opened 3 s later. The mouse was then allowed to freely explore the entire apparatus for 10 min. The movement of mice was tracked and recorded by real-time video-tracking computer software (Smart Version 2.5) linked to an overhead video camera. The total duration in the light box was measured. The apparatus was thoroughly cleaned with 70% ethanol after each trial. All data are shown as mean ± SEM and analyzed using two-tailed, unpaired Student's *t* tests.

Golgi–Cox staining

At 13 wk of age, 16 mice ($n = 8$ per group) were perfused first with phosphate-buffered saline and then with 4% paraformaldehyde. For Golgi staining, we used the FD Rapid Golgi staining kit (FD Neuro Technologies) following the manufacturer's protocol. Coronal brain slices were prepared with

a vibratome (Leica) at a thickness of 100 µm and mounted on gelatin-coated microscope slides. Images of dorsal hippocampal regions were taken with an Olympus Fluoview 1000 confocal microscope and analyzed in a blinded manner using ImageJ (National Institutes of Health). At least three neurons per animal (pyramidal neurons in the CA1 region and granule cells in the DG) were selected for quantification. Spine length and density were analyzed in >10-µm segments of secondary and third apical dendrite images or primary and secondary basal dendrite images obtained from each dendrite image within a single focal plane at 63× magnification. For apical dendrites, 10-µm segments 100–150 µm from the cell soma were randomly selected and assessed. For basal dendrites, spines were also scored along 10-µm segments located 50 to 100 µm from the soma. The types of spines were divided into four categories (thin, mushroom, stubby, and branched) based on the approximate measurements according to previously described criteria (Harris et al., 1992). In brief, types of spines were defined as follows: thin (the length was greater than the neck diameter, and the diameters of the head and neck were similar), mushroom (diameter of the head was much greater than the diameter of the neck), stubby (the diameter of the neck was similar to the total length of the spine), and branched (it has more than one head). The dendritic branching patterns were analyzed using Sholl's method (Sholl, 1953). 40× magnification images (Z-stack with 1-µm intervals) of pyramidal neurons in dorsal CA1 were captured, and each neuron was reconstructed using Adobe Photoshop CS6 and Image J (National Institutes of Health). Images were subjected to Sholl analysis using Image J (National Institutes of Health) with a starting radius of 10 µm and radius increments of 10 µm ending at 140 µm.

PSDs

200-µm brain sections containing the hippocampal CA1 region were prepared from 12-wk-old WT and *VRK3*-KO mice and fixed with 2% paraformaldehyde and 2% glutaraldehyde containing 0.05 M sodium cacodylate buffer, pH 7.2, at 4°C for 4 h. Prefixed samples were washed with 0.05 M sodium cacodylate buffer, pH 7.2, and postfixed with 1% osmium tetroxide at 4°C for 2 h. After washing briefly with distilled water, the fixed samples were treated with 0.5% uranyl acetate at 4°C for 30 min, exchanged in graded ethanol, and infiltrated with a graded series of propylene oxide and Spurr's resin mixtures. Infiltrated samples were polymerized at 70°C for 24 h. Ultrasections were obtained using an ultramicrotome (MT-X, RMC) and stained with 2% uranyl acetate and Reynolds' lead citrate. Images were obtained using a JEM-1011 electron microscope (JEOL).

PSD fractionation

The PSD fractionation procedure was performed as described previously (Bermejo et al., 2014), with minor modifications. In brief, tissue from mouse brain was homogenized in Hepes-buffered sucrose (320 mM sucrose and 5 mM Hepes, pH 7.4) containing protease inhibitor mixture (Roche) using a Teflon douncer. The homogenate was centrifuged at 1,000 *g* for 15 min at 4°C to remove cell debris and nuclei. The supernatant was spun for 20 min at 25,000 *g* to obtain the soluble and crude synaptosomal fraction. This fraction was resuspended in Hepes-buffered sucrose solution and fractionated by sucrose density-gradient centrifugation (0.8/1.0/1.2 sucrose) at 200,000 *g* for 2 h at 4°C. Purified synaptosomes/synaptic plasma membranes were collected at the 1.0–1.2-M interface. To obtain the one-triton–extracted PSD fraction, synaptosomes were resuspended in 5 vol 1 mM Tris, pH 8.1, rotated for 15 min at 4°C in buffer containing 0.5% Triton X-100/Hepes/EDTA solution, and centrifuged at 33,000 *g* for 30 min. The resulting pellet was resuspended in 50 mM Hepes/2 mM EDTA solution and stored at −80°C until it was used for Western blotting.

Immunoblotting

Hippocampi were homogenized in 1 × cell lysis buffer (20 mM Tris, 150 mM NaCl, 1 mM EDTA, 1 mM EGTA, 1% Triton-X 100, 2.5 mM sodium pyrophosphate, 1 mM β-glycerophosphate, 1 mM Na_3VO_4, 10% glycerol, 1 µg/ml leupeptin), and samples were sonicated and centrifuged at 15,000 rpm for 30 min at 4°C. The supernatant was removed, and the protein concentration was determined using Bradford reagent (Amresco). Samples were denatured for 5 min at 95°C with SDS sample buffer containing β-mercaptoethanol. Proteins were separated by SDS-PAGE and transferred to nitrocellulose membranes and proved with the indicated antibodies. The immunoblots were quantified using ImageJ software. VRK3 antiserum was generated according to an established protocol (Kang and Kim, 2006; WB 1:100). Other antibodies specific for β-galactosidase (Z378A, WB 1:1,000; Promega), CaMKII (M-176; 9035, WB 1:1,000; Santa Cruz Biotechnology), pCaMKII (Thr286; 12886, WB 1:1,000; Santa Cruz Biotechnology), p44/42 MAPK (Erk1/2; 9102, WB 1:1,000; Cell Signaling), phospho-p44/42 MAPK (Erk1/2; Thr202/Tyr204; 4695, WB 1:1,000; Cell Signaling), mTOR (2972, WB 1:1,000; Cell Signaling), phospho-mTOR (S2448; 2971, WB 1:1,000; Cell Signaling), phospho-p70 S6 kinase (Thr421/Ser424; 9204, WB 1:1,000; Cell Signaling), p70 S6 kinase (9202, WB 1:1,000; Cell Signaling), 14-3-3ζ (1019, WB 1:1,000; Santa Cruz Biotechnology), α-tubulin (5286, WB 1:1,000; Santa Cruz Biotechnology), syntaxin (7562, WB 1:1,000; Santa Cruz Biotechnology), Arc (SYSY 156 003, WB 1:1,000; Synaptic Systems), SynGAP (R-19; 8572, WB 1:1,000; Santa Cruz Biotechnology), Homer1 (ABN37, WB 1:1,000; Millipore), PAK3 (2609, WB 1:1,000; Cell Signaling), SAP97 (2D11; 9961, WB 1:1,000; Santa Cruz Biotechnology), PSD-95 (18258, WB 1:1,000; Abcam), GluR1 (82211, WB 1:1,000; Abcam), GluN1 (PA3-102, WB 1:1,000; Thermo Fisher Scientific), GluN2A (1468, WB 1:1,000; Santa Cruz Biotechnology), GluN2B (1469, WB 1:1,000; Santa Cruz Biotechnology), GluA1 (182 003, WB 1:1,000; Synaptic Systems), GluA2 (AB1768, WB 1:1,000; Millipore), GluA3 (MAB5416,

WB 1:1,000; Millipore), TrkB (80E3; 4603, WB 1:1,000; Cell Signaling), and pTrkB (Tyr 706; 135645, WB 1:1,000; Santa Cruz Biotechnology) were used.

Hippocampal slice preparation

Transverse hippocampal slices (300 µm for whole-cell patch-clamp recordings and 400 µm for extracellular field potential recordings) were prepared from 3–4-wk-old and 6–7-wk-old (rectification experiment) WT or *VRK3*-KO littermate mice (male only) as described previously (Seo et al., 2012; Choi et al., 2015). In brief, brains were isolated rapidly and placed in ice-cold, oxygenated (95% O_2 and 5% CO_2) low-Ca^{2+}/high-Mg^{2+} dissection buffer containing 5 mM KCl, 1.23 mM NaH_2PO_4, 26 mM $NaHCO_3$, 10 mM dextrose, 0.5 mM $CaCl_2$, 10 mM $MgCl_2$, and 212.7 mM sucrose. Slices were incubated in oxygenated (95% O_2 and 5% CO_2) artificial cerebrospinal fluid (ACSF) containing 124 mM NaCl, 5 mM KCl, 1.23 mM NaH_2PO_4, 2.5 mM $CaCl_2$, 1.5 mM $MgCl_2$, 26 mM $NaHCO_3$, and 10 mM dextrose at 28–30°C for at least 1 h before recording.

Extracellular field potential recordings

After recovery, slices were transferred to a recording chamber, where they were perfused continuously with oxygenated ACSF (27–28°C) at a flow rate of 2 ml/min. fEPSPs in the CA1 area were elicited by hippocampal SC stimulation (0.2-ms current pulses) using a concentric bipolar electrode. Synaptic responses recorded by ACSF-filled microelectrodes (1–3 MΩ) were quantified by the initial slope of the fEPSP. Recordings were performed using an AM-1800 microelectrode amplifier (A-M Systems), PG 4000A stimulator (Cygnus Technology), and SIU-90 isolated current source (Cygnus Technology). Baseline responses were collected at 0.07 Hz with a stimulation intensity that yielded a 40–60% maximal response. NMDA receptor–dependent LTP was induced by four episodes of theta-burst stimulation at 10-s intervals. Theta-burst stimulation consisted of 10 stimulus trains delivered at 5 Hz; each train consisted of four pulses at 100 Hz. NMDA receptor–dependent LTD was induced by single-pulse low-frequency stimulation consisting of 900 pulses at 1 Hz for 900 s. Group I mGluR-dependent LTD was induced by a 10-min bath application of 100 µM (R,S)-3,5-DHPG (Tocris Bioscience). Data from slices with stable recordings (<5% change over the baseline period) were included in the analysis. All data are presented as mean ± SEM normalized to the preconditioning baseline (at least 20 min of stable responses). The experimenters were blind to mouse genotype. IGOR software (Wavemetrics) was used for digitizing and analyzing the responses.

Whole-cell patch-clamp recordings

Slices were transferred to a recording chamber, where they were perfused continuously with oxygenated ACSF (23–25°C) at a flow rate of 2 ml/min. Slices were equilibrated for 5 min before recordings. All recordings were performed in hippocampal CA1 pyramidal neurons, which were identified by their size and morphology. Patch pipettes (4–6 MΩ) were filled with 130 mM Cs-$MeSO_4$, 0.5 mM EGTA, 5 mM TEA-Cl, 8 mM NaCl, 10 mM Hepes, 1 mM QX-314, 4 mM ATP-Mg, 0.4 mM GTP-Na, 10 mM phosphocreatine-Na2, and 0.1 mM Spermine (for the mEPSC, sEPSC, and evoked EPSC experiments), 130 mM CsCl, 1.1 mM EGTA, 2 mM $MgCl_2$, 0.1 mM $CaCl_2$, 10 mM NaCl, 10 mM Hepes, 2 mM ATP-Na (for mIPSC and sIPSC experiments), 145 mM K-gluconate, 5 NaCl, 10 mM Hepes, 0.2 EGTA, 1 $MgCl_2$, 2 ATP-Mg, and 0.1 GTP-Na (for excitability experiments) at a pH of 7.4 and 280–290 mOsm. The extracellular recording solution consisted of ACSF supplemented with 100 µM picrotoxin, 1 µM TTX, and 50 µM DL-AP5 for mEPSC experiments; 100 µM picrotoxin for the sEPSC and evoked EPSC experiment; 1 µM TTX, 20 µM CNQX, and 50 µM DL-AP5 for the mIPSC experiment; and 20 µM CNQX and 50 µM DL-AP5 for the sIPSC experiment. Neuronal excitability was measured by injecting step depolarizing currents for 500 ms. All evoked EPSCs were elicited by SC stimulation (0.1-ms current pulses) at 0.07 Hz using a concentric bipolar electrode placed 200–300 µm in front of postsynaptic pyramidal cells, and these experiments were conducted in external solution containing elevated divalent cations (4 mM Ca^{2+} and Mg^{2+}) to reduce network excitability and prevent polysynaptic responses upon stimulation (Clem and Huganir, 2010). For the experiments testing paired-pulse responses, the AMPA/NMDA ratio, and the current–voltage relationship of AMPA receptors, we evoked EPSCs by applying stimulations at half-maximal intensity (80–100 pA). The paired-pulse responses were obtained by two closely separated stimulations at 50-ms interstimulus intervals. The paired pulse ratio was depicted by the amplitude ratio of second EPSP/first EPSP. For AMPA/NMDA ratio experiments, CA1 pyramidal neurons were initially held at −70 mV, and 10 AMPA receptor–mediated EPSCs were evoked. After recording AMPA receptor–mediated EPSCs, 20 µM CNQX was added to the ACSF, and the holding potential was changed to +40 mV to record NMDA receptor–mediated EPSCs. The AMPA/NMDA ratio was calculated by dividing the mean value of 10 AMPA receptor–mediated EPSC peak amplitudes by the mean value of 10 NMDA receptor-mediated EPSC peak amplitudes. To verify the current-voltage relationship of AMPA receptors in hippocampal SC-CA1 synapses in WT or *VRK3*-KO mice, recordings were made with 50 µM of the NMDA receptor antagonist DL-AP5 in the external solution. EPSCs were evoked at multiple holding potentials (−70, −60, −40, −20, 0, +20, and +40 mV). Data were acquired using an EPC-8 amplifier (HEKA) or Multiclamp 700B amplifier (Molecular Devices), filtered at 2 kHz and digitized at 10 kHz with Digidata 1440A or 1550B1 (Molecular Devices), and analyzed using pClamp 10.2 (Molecular Devices). Only cells with access resistance <20 MΩ and input resistance >100 MΩ were studied. Cells were discarded if the input or access resistance changed by more than 20%.

Pharmacological treatment

7,8-DHF was purchased from Sigma (D5446), dissolved in phosphate-buffered saline containing 17% DMSO to a final concentration of 10 mg/kg, and administered by intraperitoneal injection at a volume of 0.01 ml/g. For transient treatment, 7,8-DHF was administered to 12-wk-old mice once daily for three consecutive days, and mice were subjected to behavioral tests 1 and 7 d after treatment (Fig. 8 and Fig. 10, A and B). For chronic treatment, 7,8-DHF was administered to 4-wk-old mice at 1-wk intervals until mice reached 11 wk of age, and behavioral tests were performed at 12, 16, and 24 wk of age (Fig. 9 and Fig. 10, C–F). For electrophysiological experiments, 7,8-DHF was suspended to a 10 mM concentration in DMSO and diluted 1:1,000 in external solution; therefore, final concentration to treat 7,8-DHF is 10 μM with 0.1% DMSO. Vehicle solution was composed of same one described previously but excluding 10 μM 7,8-DHF.

Statistical analysis

All data are shown as mean ± SEM and analyzed using χ^2 tests, unpaired two-sided Student's *t* tests, one-way ANOVA with Turkey's post-hoc tests, or two-way ANOVA with Bonferroni's post-hoc tests. For Sholl analysis of dendritic complexity, we used a repeated-measures two-way ANOVA with genotype and radius as factors. All statistical analyses were performed using Prism 4 (GraphPad), Microsoft Office (for graphical display, version 15.0.4569.1506; Microsoft), or SigmaPlot (for statistical analysis, version 11.0; Systat Software).

Online supplemental material

Fig. S1 shows the gene trap insertion site and the effect on VRK3 protein. Fig. S2 shows that *VRK3* mutant mice exhibit impaired learning and memory performance along with hyperactivity and anxiolytic behavior. Fig. S3 shows the normal basal synaptic transmission and metabotropic glutamate receptor-induced LTD in *VRK3*-KO mice. Fig. S4 shows the biochemical changes in the hippocampal PSD fraction and whole lysates of young *VRK3*-KO mice. Fig. S5 shows the restorative effects of 7,8-DHF on the deficits in learning and memory in *VRK3*-KO mice.

ACKNOWLEDGMENTS

We are grateful to Dr. Sung Han (Salk Institute, USA) for critical reading of the manuscript and helpful advice, Drs. Bo-Hwa Choi and Hoe-Yune Jung (Pohang Technopark, Korea) for providing a facility for behavioral experiments, and Dr. Yong Ryoul Yang (Ulsan National Institute of Science and Technology, Korea) for helpful advice and discussions. We also thank Y.G. Kim for animal maintenance.

This study makes use of data generated by the DECIPHER Consortium (supported by the Wellcome Trust), and a full list of centers who contributed to the generation of the data is available online (http://decipher.sanger.ac.uk) or via email (decipher@sanger.ac.uk). This work was supported by the National Research Foundation of Korea (Basic Research Laboratory program grant 2014054324 and the Brain Korea 21 plus program grant 10Z20130012243), the Cooperative Research Program for Agriculture Science and Technology Development (PJ01121602), which is funded by the Rural Development Administration, and the Green Science project, which is funded by POSCO, Republic of Korea. This research was also supported by the Brain Research Program through the National Research Foundation of Korea (NRF) funded by the Ministry of Science, ICT and Future Planning (2017023478).

The authors declare no competing financial interests.

Author contributions: K.-T. Kim and M.-S. Kang designed the research. M.-S. Kang performed behavior and biochemical experiments. T.-Y. Choi and S.-H. Lee performed electrophysiology and analyzed data. H.G. Ryu performed EM image acquisition and analyzed data. D. Lee performed qRT-PCR and analyzed data. M.-S. Kang, K.-T. Kim, and S.-Y. Choi wrote the manuscript. K.-T. Kim supervised the project.

Submitted: 26 June 2016
Revised: 12 December 2016
Accepted: 9 February 2017

REFERENCES

Anggono, V., and R.L. Huganir. 2012. Regulation of AMPA receptor trafficking and synaptic plasticity. *Curr. Opin. Neurobiol.* 22:461–469. http://dx.doi.org/10.1016/j.conb.2011.12.006

Bennett, M.R., and J. Lagopoulos. 2014. Stress and trauma: BDNF control of dendritic-spine formation and regression. *Prog. Neurobiol.* 112:80–99. http://dx.doi.org/10.1016/j.pneurobio.2013.10.005

Bermejo, M.K., M. Milenkovic, A. Salahpour, and A.J. Ramsey. 2014. Preparation of synaptic plasma membrane and postsynaptic density proteins using a discontinuous sucrose gradient. *J. Vis. Exp.* 91:e51896. http://dx.doi.org/10.3791/51896

Blundell, J., C.A. Blaiss, M.R. Etherton, F. Espinosa, K. Tabuchi, C. Walz, M.F. Bolliger, T.C. Südhof, and C.M. Powell. 2010. Neuroligin-1 deletion results in impaired spatial memory and increased repetitive behavior. *J. Neurosci.* 30:2115–2129. http://dx.doi.org/10.1523/JNEUROSCI.4517-09.2010

Bult, C.J., J.A. Kadin, J.E. Richardson, J.A. Blake, J.T. Eppig, and G. Mouse Genome Database. Mouse Genome Database Group. 2010. The Mouse Genome Database: Enhancements and updates. *Nucleic Acids Res.* 38:D586–D592. http://dx.doi.org/10.1093/nar/gkp880

Cao, C., M.S. Rioult-Pedotti, P. Migani, C.J. Yu, R. Tiwari, K. Parang, M.R. Spaller, D.J. Goebel, and J. Marshall. 2013. Impairment of TrkB-PSD-95 signaling in Angelman syndrome. *PLoS Biol.* 11:e1001478. (published erratum appears in *PLoS Biol.* 2014. 12:e1001848) http://dx.doi.org/10.1371/journal.pbio.1001478

Caroni, P., F. Donato, and D. Muller. 2012. Structural plasticity upon learning: Regulation and functions. *Nat. Rev. Neurosci.* 13:478–490. http://dx.doi.org/10.1038/nrn3258

Chahrour, M., and H.Y. Zoghbi. 2007. The story of Rett syndrome: From clinic to neurobiology. *Neuron.* 56:422–437. http://dx.doi.org/10.1016/j.neuron.2007.10.001

Chao, M.V. 2003. Neurotrophins and their receptors: A convergence point for many signalling pathways. *Nat. Rev. Neurosci.* 4:299–309. http://dx.doi.org/10.1038/nrn1078

Chao, H.T., H. Chen, R.C. Samaco, M. Xue, M. Chahrour, J. Yoo, J.L. Neul, S. Gong, H.C. Lu, N. Heintz, et al. 2010. Dysfunction in GABA signalling mediates autism-like stereotypies and Rett syndrome phenotypes. *Nature.* 468:263–269. http://dx.doi.org/10.1038/nature09582

Choi, T.Y., S. Jung, J. Nah, H.Y. Ko, S.H. Jo, G. Chung, K. Park, Y.K. Jung, and S.Y. Choi. 2015. Low levels of methyl β-cyclodextrin disrupt GluA1-dependent synaptic potentiation but not synaptic depression. *J. Neurochem.* 132:276–285. http://dx.doi.org/10.1111/jnc.12995

Chung, W., S.Y. Choi, E. Lee, H. Park, J. Kang, H. Park, Y. Choi, D. Lee, S.G. Park, R. Kim, et al. 2015. Social deficits in IRSp53 mutant mice improved by NMDAR and mGluR5 suppression. *Nat. Neurosci.* 18:435–443. http://dx.doi.org/10.1038/nn.3927

Clem, R.L., and R.L. Huganir. 2010. Calcium-permeable AMPA receptor dynamics mediate fear memory erasure. *Science.* 330:1108–1112. http://dx.doi.org/10.1126/science.1195298

Delorme, R., E. Ey, R. Toro, M. Leboyer, C. Gillberg, and T. Bourgeron. 2013. Progress toward treatments for synaptic defects in autism. *Nat. Med.* 19:685–694. http://dx.doi.org/10.1038/nm.3193

Ebert, D.H., and M.E. Greenberg. 2013. Activity-dependent neuronal signalling and autism spectrum disorder. *Nature.* 493:327–337. http://dx.doi.org/10.1038/nature11860

Faridar, A., D. Jones-Davis, E. Rider, J. Li, I. Gobius, L. Morcom, L.J. Richards, S. Sen, and E.H. Sherr. 2014. Mapk/Erk activation in an animal model of social deficits shows a possible link to autism. *Mol. Autism.* 5:57. http://dx.doi.org/10.1186/2040-2392-5-57

Firth, H.V., S.M. Richards, A.P. Bevan, S. Clayton, M. Corpas, D. Rajan, S. Van Vooren, Y. Moreau, R.M. Pettett, and N.P. Carter. 2009. DECIPHER: Database of Chromosomal Imbalance and Phenotype in Humans Using Ensembl Resources. *Am. J. Hum. Genet.* 84:524–533. http://dx.doi.org/10.1016/j.ajhg.2009.03.010

Flavell, S.W., and M.E. Greenberg. 2008. Signaling mechanisms linking neuronal activity to gene expression and plasticity of the nervous system. *Annu. Rev. Neurosci.* 31:563–590. http://dx.doi.org/10.1146/annurev.neuro.31.060407.125631

Fortin, D.A., T. Srivastava, D. Dwarakanath, P. Pierre, S. Nygaard, V.A. Derkach, and T.R. Soderling. 2012. Brain-derived neurotrophic factor activation of CaM-kinase kinase via transient receptor potential canonical channels induces the translation and synaptic incorporation of GluA1-containing calcium-permeable AMPA receptors. *J. Neurosci.* 32:8127–8137. http://dx.doi.org/10.1523/JNEUROSCI.6034-11.2012

Han, S., C. Tai, R.E. Westenbroek, F.H. Yu, C.S. Cheah, G.B. Potter, J.L. Rubenstein, T. Scheuer, H.O. de la Iglesia, and W.A. Catterall. 2012. Autistic-like behaviour in Scn1a+/- mice and rescue by enhanced GABA-mediated neurotransmission. *Nature.* 489:385–390. http://dx.doi.org/10.1038/nature11356

Harris, K.M., F.E. Jensen, and B. Tsao. 1992. Three-dimensional structure of dendritic spines and synapses in rat hippocampus (CA1) at postnatal day 15 and adult ages: Implications for the maturation of synaptic physiology and long-term potentiation. *J. Neurosci.* 12:2685–2705.

Huang, N., I. Lee, E.M. Marcotte, and M.E. Hurles. 2010. Characterising and predicting haploinsufficiency in the human genome. *PLoS Genet.* 6:e1001154. http://dx.doi.org/10.1371/journal.pgen.1001154

Hullinger, R., M. Li, J. Wang, Y. Peng, J.A. Dowell, E. Bomba-Warczak, H.A. Mitchell, C. Burger, E.R. Chapman, J.M. Denu, et al. 2016. Increased expression of AT-1/SLC33A1 causes an autistic-like phenotype in mice by affecting dendritic branching and spine formation. *J. Exp. Med.* 213:1267–1284. http://dx.doi.org/10.1084/jem.20151776

Ji, Y., Y. Lu, F. Yang, W. Shen, T.T. Tang, L. Feng, S. Duan, and B. Lu. 2010. Acute and gradual increases in BDNF concentration elicit distinct signaling and functions in neurons. *Nat. Neurosci.* 13:302–309. http://dx.doi.org/10.1038/nn.2505

Johnson, R.A., M. Lam, A.M. Punzo, H. Li, B.R. Lin, K. Ye, G.S. Mitchell, and Q. Chang. 2012. 7,8-dihydroxyflavone exhibits therapeutic efficacy in a mouse model of Rett syndrome. *J. Appl. Physiol.* 112:704–710. http://dx.doi.org/10.1152/japplphysiol.01361.2011

Jurado, S., D. Goswami, Y. Zhang, A.J. Molina, T.C. Südhof, and R.C. Malenka. 2013. LTP requires a unique postsynaptic SNARE fusion machinery. *Neuron.* 77:542–558. http://dx.doi.org/10.1016/j.neuron.2012.11.029

Kang, T.H., and K.T. Kim. 2006. Negative regulation of ERK activity by VRK3-mediated activation of VHR phosphatase. *Nat. Cell Biol.* 8:863–869. http://dx.doi.org/10.1038/ncb1447

Kaphzan, H., P. Hernandez, J.I. Jung, K.K. Cowansage, K. Deinhardt, M.V. Chao, T. Abel, and E. Klann. 2012. Reversal of impaired hippocampal long-term potentiation and contextual fear memory deficits in Angelman syndrome model mice by ErbB inhibitors. *Biol. Psychiatry.* 72:182–190. http://dx.doi.org/10.1016/j.biopsych.2012.01.021

Kelleher, R.J. III, and M.F. Bear. 2008. The autistic neuron: Troubled translation? *Cell.* 135:401–406. http://dx.doi.org/10.1016/j.cell.2008.10.017

Kim, J.W., H. Seung, K.C. Kim, E.L. Gonzales, H.A. Oh, S.M. Yang, M.J. Ko, S.H. Han, S. Banerjee, and C.Y. Shin. 2017. Agmatine rescues autistic behaviors in the valproic acid-induced animal model of autism. *Neuropharmacology.* 113:71–81. http://dx.doi.org/10.1016/j.neuropharm.2016.09.014

Klerkx, E.P., P.A. Lazo, and P. Askjaer. 2009. Emerging biological functions of the vaccinia-related kinase (VRK) family. *Histol. Histopathol.* 24:749–759.

Lee, E.J., S.Y. Choi, and E. Kim. 2015. NMDA receptor dysfunction in autism spectrum disorders. *Curr. Opin. Pharmacol.* 20:8–13. http://dx.doi.org/10.1016/j.coph.2014.10.007

Lin, Y.C., and A.J. Koleske. 2010. Mechanisms of synapse and dendrite maintenance and their disruption in psychiatric and neurodegenerative disorders. *Annu. Rev. Neurosci.* 33:349–378. http://dx.doi.org/10.1146/annurev-neuro-060909-153204

Lin, Y.C., J.A. Frei, M.B. Kilander, W. Shen, and G.J. Blatt. 2016. A subset of autism-associated genes regulate the structural stability of neurons. *Front. Cell. Neurosci.* 10:263. http://dx.doi.org/10.3389/fncel.2016.00263

Liu, S.J., and R.S. Zukin. 2007. Ca^{2+}-permeable AMPA receptors in synaptic plasticity and neuronal death. *Trends Neurosci.* 30:126–134. http://dx.doi.org/10.1016/j.tins.2007.01.006

Lu, B., G. Nagappan, X. Guan, P.J. Nathan, and P. Wren. 2013. BDNF-based synaptic repair as a disease-modifying strategy for neurodegenerative diseases. *Nat. Rev. Neurosci.* 14:401–416. http://dx.doi.org/10.1038/nrn3505

Minichiello, L. 2009. TrkB signalling pathways in LTP and learning. *Nat. Rev. Neurosci.* 10:850–860. http://dx.doi.org/10.1038/nrn2738

Nadler, J.J., S.S. Moy, G. Dold, D. Trang, N. Simmons, A. Perez, N.B. Young, R.P. Barbaro, J. Piven, T.R. Magnuson, and J.N. Crawley. 2004. Automated apparatus for quantitation of social approach behaviors in mice. *Genes Brain Behav.* 3:303–314. http://dx.doi.org/10.1111/j.1601-183X.2004.00071.x

Park, C.H., H.G. Ryu, S.H. Kim, D. Lee, H. Song, and K.T. Kim. 2015. Presumed pseudokinase VRK3 functions as a BAF kinase. *Biochim. Biophys. Acta.* 1853:1738–1748. http://dx.doi.org/10.1016/j.bbamcr.2015.04.007

Peça, J., C. Feliciano, J.T. Ting, W. Wang, M.F. Wells, T.N. Venkatraman, C.D. Lascola, Z. Fu, and G. Feng. 2011. Shank3 mutant mice display autistic-like behaviours and striatal dysfunction. *Nature.* 472:437–442. http://dx.doi.org/10.1038/nature09965

Pelka, G.J., C.M. Watson, T. Radziewic, M. Hayward, H. Lahooti, J. Christodoulou, and P.P. Tam. 2006. Mecp2 deficiency is associated with learning and cognitive deficits and altered gene activity in the hippocampal region of mice. *Brain.* 129:887–898. http://dx.doi.org/10.1093/brain/awl022

Qureshi, A.Y., S. Mueller, A.Z. Snyder, P. Mukherjee, J.I. Berman, T.P. Roberts, S.S. Nagarajan, J.E. Spiro, W.K. Chung, E.H. Sherr, and R.L. Buckner. Simons VIP Consortium. 2014. Opposing brain differences in 16p11.2 deletion and duplication carriers. *J. Neurosci.* 34:11199–11211. http://dx.doi.org/10.1523/JNEUROSCI.1366-14.2014

Renbaum, P., E. Kellerman, R. Jaron, D. Geiger, R. Segel, M. Lee, M.C. King, and E. Levy-Lahad. 2009. Spinal muscular atrophy with pontocerebellar hypoplasia is caused by a mutation in the VRK1 gene. *Am. J. Hum. Genet.* 85:281–289. http://dx.doi.org/10.1016/j.ajhg.2009.07.006

Sala, C., K. Futai, K. Yamamoto, P.F. Worley, Y. Hayashi, and M. Sheng. 2003. Inhibition of dendritic spine morphogenesis and synaptic transmission by activity-inducible protein Homer1a. *J. Neurosci.* 23:6327–6337.

Santos, A.R., D. Comprido, and C.B. Duarte. 2010. Regulation of local translation at the synapse by BDNF. *Prog. Neurobiol.* 92:505–516. http://dx.doi.org/10.1016/j.pneurobio.2010.08.004

Sebollela, A., L. Freitas-Correa, F.F. Oliveira, A.C. Paula-Lima, L.M. Saraiva, S.M. Martins, L.D. Mota, C. Torres, S. Alves-Leon, J.M. de Souza, et al. 2012. Amyloid-β oligomers induce differential gene expression in adult human brain slices. *J. Biol. Chem.* 287:7436–7445. http://dx.doi.org/10.1074/jbc.M111.298471

Seo, J., K. Kim, S. Jang, S. Han, S.Y. Choi, and E. Kim. 2012. Regulation of hippocampal long-term potentiation and long-term depression by diacylglycerol kinase ζ. *Hippocampus.* 22:1018–1026. http://dx.doi.org/10.1002/hipo.20889

Sholl, D.A. 1953. Dendritic organization in the neurons of the visual and motor cortices of the cat. *J. Anat.* 87:387–406.

Silverman, J.L., M. Yang, C. Lord, and J.N. Crawley. 2010. Behavioural phenotyping assays for mouse models of autism. *Nat. Rev. Neurosci.* 11:490–502. http://dx.doi.org/10.1038/nrn2851

Sohn, H., B. Kim, K.H. Kim, M.K. Kim, T.K. Choi, and S.H. Lee. 2014. Effects of VRK2 (rs2312147) on white matter connectivity in patients with schizophrenia. *PLoS One.* 9:e103519. http://dx.doi.org/10.1371/journal.pone.0103519

Stryke, D., M. Kawamoto, C.C. Huang, S.J. Johns, L.A. King, C.A. Harper, E.C. Meng, R.E. Lee, A. Yee, L. L'Italien, et al. 2003. BayGenomics: A resource of insertional mutations in mouse embryonic stem cells. *Nucleic Acids Res.* 31:278–281. http://dx.doi.org/10.1093/nar/gkg064

Subramanian, M., C.K. Timmerman, J.L. Schwartz, D.L. Pham, and M.K. Meffert. 2015. Characterizing autism spectrum disorders by key biochemical pathways. *Front. Neurosci.* 9:313. http://dx.doi.org/10.3389/fnins.2015.00313

Sztainberg, Y., and H.Y. Zoghbi. 2016. Lessons learned from studying syndromic autism spectrum disorders. *Nat. Neurosci.* 19:1408–1417. http://dx.doi.org/10.1038/nn.4420

Thomas, G.M., and R.L. Huganir. 2004. MAPK cascade signalling and synaptic plasticity. *Nat. Rev. Neurosci.* 5:173–183. http://dx.doi.org/10.1038/nrn1346

Tian, M., Y. Zeng, Y. Hu, X. Yuan, S. Liu, J. Li, P. Lu, Y. Sun, L. Gao, D. Fu, et al. 2015. 7, 8-Dihydroxyflavone induces synapse expression of AMPA GluA1 and ameliorates cognitive and spine abnormalities in a mouse model of fragile X syndrome. *Neuropharmacology.* 89:43–53. http://dx.doi.org/10.1016/j.neuropharm.2014.09.006

van Woerden, G.M., K.D. Harris, M.R. Hojjati, R.M. Gustin, S. Qiu, R. de Avila Freire, Y.H. Jiang, Y. Elgersma, and E.J. Weeber. 2007. Rescue of neurological deficits in a mouse model for Angelman syndrome by reduction of alphaCaMKII inhibitory phosphorylation. *Nat. Neurosci.* 10:280–282. http://dx.doi.org/10.1038/nn1845

von Bohlen und Halbach, O., S. Krause, D. Medina, C. Sciarretta, L. Minichiello, and K. Unsicker. 2006. Regional- and age-dependent reduction in trkB receptor expression in the hippocampus is associated with altered spine morphologies. *Biol. Psychiatry.* 59:793–800. http://dx.doi.org/10.1016/j.biopsych.2005.08.025

Wang, I.T., M. Allen, D. Goffin, X. Zhu, A.H. Fairless, E.S. Brodkin, S.J. Siegel, E.D. Marsh, J.A. Blendy, and Z. Zhou. 2012. Loss of CDKL5 disrupts kinome profile and event-related potentials leading to autistic-like phenotypes in mice. *Proc. Natl. Acad. Sci. USA.* 109:21516–21521. http://dx.doi.org/10.1073/pnas.1216988110

Weeber, E.J., Y.H. Jiang, Y. Elgersma, A.W. Varga, Y. Carrasquillo, S.E. Brown, J.M. Christian, B. Mirnikjoo, A. Silva, A.L. Beaudet, and J.D. Sweatt. 2003. Derangements of hippocampal calcium/calmodulin-dependent protein kinase II in a mouse model for Angelman mental retardation syndrome. *J. Neurosci.* 23:2634–2644.

Whitehead, G., P. Regan, D.J. Whitcomb, and K. Cho. 2017. Ca^{2+}-permeable AMPA receptor: A new perspective on amyloid-beta mediated pathophysiology of Alzheimer's disease. *Neuropharmacology.* 112(Pt A):221–227. http://dx.doi.org/10.1016/j.neuropharm.2016.08.022

Won, H., H.R. Lee, H.Y. Gee, W. Mah, J.I. Kim, J. Lee, S. Ha, C. Chung, E.S. Jung, Y.S. Cho, et al. 2012. Autistic-like social behaviour in Shank2-mutant mice improved by restoring NMDA receptor function. *Nature.* 486:261–265. http://dx.doi.org/10.1038/nature11208

Wu, G.Y., K. Deisseroth, and R.W. Tsien. 2001. Spaced stimuli stabilize MAPK pathway activation and its effects on dendritic morphology. *Nat. Neurosci.* 4:151–158. http://dx.doi.org/10.1038/83976

Xu, L.M., J.R. Li, Y. Huang, M. Zhao, X. Tang, and L. Wei. 2012. AutismKB: An evidence-based knowledgebase of autism genetics. *Nucleic Acids Res.* 40(D1):D1016–D1022. http://dx.doi.org/10.1093/nar/gkr1145

Yashiro, K., T.T. Riday, K.H. Condon, A.C. Roberts, D.R. Bernardo, R. Prakash, R.J. Weinberg, M.D. Ehlers, and B.D. Philpot. 2009. Ube3a is required for experience-dependent maturation of the neocortex. *Nat. Neurosci.* 12:777–783. http://dx.doi.org/10.1038/nn.2327

Yufune, S., Y. Satoh, I. Takamatsu, H. Ohta, Y. Kobayashi, Y. Takaenoki, G. Pagès, J. Pouysségur, S. Endo, and T. Kazama. 2015. Transient blockade of ERK phosphorylation in the critical period causes autistic phenotypes as an adult in mice. *Sci. Rep.* 5:10252. http://dx.doi.org/10.1038/srep10252